

A superconvergent alpha finite element method ($S\alpha$ FEM) for static and free vibration analysis of shell structures

Yingbin Chai ^{a,b}, Wei Li ^{a,b,c,*}, Guirong Liu ^d, Zhixiong Gong ^{a,b}, Tianyun Li ^{a,b,c}

^a School of Naval Architecture and Ocean Engineering, Huazhong University of Science and Technology, Wuhan 430074, China

^b Hubei Key Laboratory of Naval Architecture and Ocean Engineering Hydrodynamics (HUST), Huazhong University of Science and Technology, Wuhan 430074, China

^c Collaborative Innovation Center for Advanced Ship and Deep-Sea Exploration (CISSE), Shanghai 200240, China

^d Department of Aerospace Engineering and Engineering Mechanics, University of Cincinnati, OH 45221-0070, USA



ARTICLE INFO

Article history:

Received 24 July 2016

Accepted 24 October 2016

Available online 14 November 2016

Keywords:

Numerical methods

Alpha finite element method (α FEM)

Discrete shear gap technique (DSG)

Node-based smoothed finite element

method (NS-FEM)

Strain smoothing technique

ABSTRACT

A superconvergent alpha finite element method ($S\alpha$ FEM) based on triangular mesh is presented for static and free vibration analysis of shell structures. In the $S\alpha$ FEM model, a linear strain field is re-constructed from the standard FEM piecewise constant strain field by devising a unique procedure with a tunable parameter α . The discretized system equations are then established based on the re-constructed strain field and the Hellinger-Reissner variational principle. By changing the value of the parameter α , our $S\alpha$ FEM can provide a proper softer stiffness leading to a “nearly exact” solution in strain energy norm. To avoid the transverse shear locking (caused by the Hellinger-Reissner theory), the discrete shear gap technique for triangular element (DSG3) is employed. From several typical numerical examples, it is demonstrated that the proposed $S\alpha$ -FEM-DSG3 (or $S\alpha$ -DSG3) possesses superconvergence property and can provide very accurate solutions for shell structures.

© 2016 Elsevier Ltd. All rights reserved.

1. Introduction

The analysis of plate and shell structures is of great importance because these structures are widely used in practical engineering systems [1–4]. During the past several decades, the well-known Rerssner-Mindlin theory has been extensively employed for constructing variety of plate and shell elements. One major simplification in the Rerssner-Mindlin theory is that only C^0 continuity is required, offering convenience in creating weakform and weakened weakform models [5]. This is in contrast to the complex implementation of C^1 continuity necessitated by the classical Kirchhoff hypothesis. In practical applications, the displacement formulation based on Reissner-Mindlin theory is the dominating model due to these computational advantages, which allows independent approximation of the deflection and the rotations. These displacement-based shell elements possess high accuracy and fast convergence speed property. However, they often result in “overly-stiff” solutions due to the use of weakform and the well-known shear locking issue. It is known that shear locking results from the same order approximation for the deflection and rotation, resulting conflicts when the thickness of plates and shells trends

to zero. Such conflicts can lead to excessive stiffness dominated by the shear deformation and hence known as shear locking. When shear locking happens, the numerical results would be erroneous. In order to deal with this, a number of techniques have been suggested with varying degree of success.

Bathe and his colleagues proposed the “mixed interpolation of tensorial components” (MITC) approach to overcome the shear locking issue. In MITC technique, the displacements and strains are interpolated separately and the separate interpolation are connected at “tying points”. In addition, the choice of these interpolations should satisfy the ellipticity and consistency conditions. Based on MITC, the 4-node shell elements (MITC4) and 8-node shell elements (MITC8) were first developed for the analysis of shell structures [6,7]. It was found that the MITC technique for quadrilateral elements can remove the shear locking issue successfully. Recently, Lee et al. have proposed a series of new MITC shell elements (including the MITC3+ shell element and MITC4+ shell element) to improve the performance of the previous MITC shell elements [8–13]. Various numerical examples demonstrate that these new MITC shell elements increase the accuracy of the solution and show excellent convergence behaviors. Hughes et al. employed the reduced and selective integration techniques to alleviate the shear locking effect [14–16]. In these integration schemes, the bending term is integrated with the “normal” rule, whereas the shear term is integrated with a lower-order rule.

* Corresponding author at: School of Naval Architecture and Ocean Engineering, Huazhong University of Science and Technology, Wuhan 430074, China.

E-mail address: hustliw@hust.edu.cn (W. Li).

Numerical results showed that the avoidance of shear locking was facilitated by the reduced and selective integration techniques and these schemes were very effective in explicit transient calculation. However, these integration techniques often lead to an instability and exhibited zero energy modes. The assumed natural strain (ANS) method was proposed by MacNeal to deal with shear locking [17]. In the ANS method, the element stiffness matrices are derived from an assumed strain field rather than an assumed displacement field. Based on the ANS method, a three-node Mindlin plate element (MIN3) was introduced by Tessler and Hughes for plate analysis [18]. In this kind of element, a quadratic field is created for deflection by continuous shear edge constraints. It was observed that the MIN3 is free of shear locking and can provide convergent solutions. Also based on the ANS method, Kim developed a three-node macro triangular shell element to attenuate the shear locking effect [19]. Various numerical examples demonstrated that this shell element can remove the shear locking effect completely and can achieve very accurate solutions. In recent years, the discrete shear gap (DSG) method was proposed by Bletzinger et al. to eliminate the shear locking problem [20]. It is based on a pure displacement formulation and utilizes only the usual displacement and rotational degrees of freedom at the nodes. The formulation of DSG needs no extra nodes and parameters and it is very easy to implement. It is observed that the DSG method is free of shear locking and works very well for triangular and rectangular elements.

Another obstacle in the development of shell elements is the “overly-stiff” behavior as a result of using the standard weak-forms. The “overly-stiff” behavior, which usually results in poor accuracy in the solution, is an inherent characteristic of the displacement-based FEM models which uses the standard Galerkin weakform. When it comes to three-node triangular shell elements, this issue will be even more severe. In order to soften the stiffness of the standard FEM models and achieve more accurate results, Liu et al. have proposed a series of smoothed finite element methods (S-FEM) [21–25] which are formulated by combining the strain smoothing techniques of meshfree methods [26] with the existing standard finite element method. In these S-FEM models, the compatible strain fields are smoothed based on the smoothing domains created from the entities of the elements mesh such as cells (cell-based S-FEM, CS-FEM [27–31]), or nodes (node-based S-FEM, NS-FEM [32–34]), or edges (edge-based S-FEM, ES-FEM [35–40]), or faces (face-based S-FEM, FS-FEM [41,42]). Among these S-FEM models, different S-FEM models possess different properties and a very nice overview of S-FEM models can be found in the textbooks [21]. The S-FEM models use a so-called weakened weakform or W2 form [5], instead of the standard weakform.

This paper aims to perform the linear, nonlinear and free vibration analysis of shell structures using a superconvergent alpha finite element method (S α FEM) [43–47]. The S α FEM was originally proposed by Liu et al. for 2D analysis of solid mechanics problems. The essential idea of S α FEM for triangular elements is to construct a novel linear strain field by combining the compatible strains in the standard FEM and the smoothed strains in the node-based smoothed finite element method (NS-FEM) with the help of an adjustable factor α . The NS-FEM can be considered as a particular form of nodal integrated techniques in the finite element formulation [48–54]. In the NS-FEM model, the smoothed strain field in the node-based smoothed smoothing domain is obtained via a weighted average of the surrounding element values. It is found that the NS-FEM works well in solving volumetric locking problems and can provide an upper bound solution to solid mechanics problems. However, the NS-FEM also suffers from the “over-soft” property and can lead to spurious non-zero energy modes for dynamic problems. In the S α FEM model presented in this paper, both the contributions from the standard FEM and the contribu-

tions from the NS-FEM are considered. Based on the Hellinger-Reissner variational principle, a novel Galerkin-like weak form is obtained for establishing the discretized system equations. This novel Galerkin-like weak form is variational consistent and possesses similar properties of the standard one. It is found that the S α FEM behaves much better than the standard FEM-T3 and even surpasses the FEM-Q4 with the same set of nodes. Our focus in this work is to further extend the S α FEM to shell analysis. In the S α FEM for shell structures, the membrane, curvature and transverse shear strains are enhanced by introducing a crucial parameter α . As a result, the obtained strain field is closer to the exact strain field than the standard one. With the aim of avoiding the transverse shear locking issue, the discrete shear gap technique for triangular element (DSG3) is employed to give a so-called superconvergent alpha the discrete shear gap (S α -FEM-DSG3 or S α -DSG3) model. From several typical numerical examples, it is demonstrated that the proposed S α -DSG3 possesses superconvergence property and can provide very accurate numerical solutions for shell structures.

The paper is organized as follows: the review of pertinent governing equations and weak form is presented in Section 2. Section 3 presents the detailed formulation of S α -DSG3 for the Reissner-Mindlin shell. In Section 4, several typical numerical examples are studied and discussed in details. Final conclusions from the numerical results are drawn in Section 5.

2. The review of pertinent formulation for classical flat shell element

It is known that the flat shell elements, which are simple but widely used shell elements, can be formulated easily by combining the 2D solid element for plane elasticity and the plate bending element for plate theory [4]. The 2D solid elements handle the membrane effects, while the plate elements are used to tackle the bending effects. Since the flat shell elements are easy to implement and computationally efficient, hence the theory of flat shell elements will be chosen to analyze the shell structures in this paper.

2.1. Governing equations and weak form

Considering a flat shell in Fig. 1 undergoes membrane and bending forces simultaneously. Based on the Reissner-Mindlin theory, the particles of the shell originally on a line that is normal to the undeformed middle surface remain on a straight line during deformation, but this line is not necessarily normal to the deformed

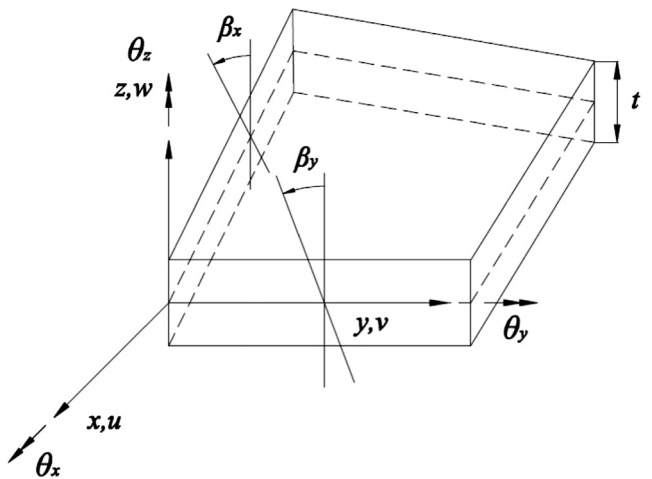


Fig. 1. The illustration of a typical flat shell element.

middle surface. With this assumption, the curvature κ and transverse shear strain γ can be defined as

$$\kappa = \begin{bmatrix} \frac{\partial \theta_y}{\partial x} \\ -\frac{\partial \theta_x}{\partial x} \\ \frac{\partial \theta_y}{\partial y} - \frac{\partial \theta_x}{\partial x} \end{bmatrix}, \quad \gamma = \begin{bmatrix} \frac{\partial w}{\partial x} + \theta_y \\ \frac{\partial w}{\partial y} - \theta_x \end{bmatrix} \quad (1)$$

where u, v, w are the displacements of the middle surface in the x, y, z directions and $\theta_x, \theta_y, \theta_z$ are the rotations respect to x, y, z directions, respectively.

For linear analysis, the membrane strain $\boldsymbol{\varepsilon}_m$ is given by:

$$\boldsymbol{\varepsilon}_m = \boldsymbol{\varepsilon}_m^l = \begin{bmatrix} \frac{\partial u}{\partial x} \\ \frac{\partial v}{\partial y} \\ \frac{\partial u}{\partial y} + \frac{\partial v}{\partial x} \end{bmatrix} \quad (2)$$

For nonlinear analysis,

$$\boldsymbol{\varepsilon}_m = \boldsymbol{\varepsilon}_m^l + \boldsymbol{\varepsilon}_m^{nl} = \begin{bmatrix} \frac{\partial u}{\partial x} \\ \frac{\partial v}{\partial y} \\ \frac{\partial u}{\partial y} + \frac{\partial v}{\partial x} \end{bmatrix} + \begin{bmatrix} \frac{1}{2} \left(\frac{\partial w}{\partial x} \right)^2 \\ \frac{1}{2} \left(\frac{\partial w}{\partial y} \right)^2 \\ \frac{\partial w}{\partial x} \frac{\partial w}{\partial y} \end{bmatrix} \quad (3)$$

in which $\boldsymbol{\varepsilon}_m^l$ and $\boldsymbol{\varepsilon}_m^{nl}$ represent the linear part and nonlinear part, respectively.

Then the constitutive relationship can be expressed as:

$$\hat{\boldsymbol{\sigma}} = \hat{\mathbf{D}} \hat{\boldsymbol{\varepsilon}} \quad (4)$$

where

$$\hat{\boldsymbol{\sigma}} = \begin{bmatrix} \hat{\mathbf{N}} \\ \hat{\mathbf{M}} \\ \hat{\mathbf{Q}} \end{bmatrix}, \quad \hat{\mathbf{D}} = \begin{bmatrix} \mathbf{D}_m & \mathbf{0} & \mathbf{0} \\ \mathbf{0} & \mathbf{D}_b & \mathbf{0} \\ \mathbf{0} & \mathbf{0} & \mathbf{D}_s \end{bmatrix}, \quad \hat{\boldsymbol{\varepsilon}} = \begin{bmatrix} \boldsymbol{\varepsilon}_m \\ \boldsymbol{\varepsilon}_b \\ \boldsymbol{\varepsilon}_s \end{bmatrix} \quad (5)$$

in which $\hat{\mathbf{N}} = [N_x \ N_y \ N_{xy}]^T$ is the membrane force vector in the mid-plane, $\hat{\mathbf{M}} = [M_x \ M_y \ M_{xy}]^T$ is the bending moment vector, $\hat{\mathbf{Q}} = [Q_x \ Q_y]^T$ is the transverse shear force vector, $\mathbf{D}_m, \mathbf{D}_b$ and \mathbf{D}_s are the related stiffness constitutive coefficients.

Applying the principle of virtual work, the standard Galerkin weak form for static problems is given by

$$\int_{\Omega} (\delta \boldsymbol{\varepsilon}_m)^T \mathbf{D}_m \boldsymbol{\varepsilon}_m d\Omega + \int_{\Omega} \delta \kappa^T \mathbf{D}_b \kappa d\Omega + \int_{\Omega} \delta \gamma^T \mathbf{D}_s \gamma d\Omega - \int_{\Omega} \delta \mathbf{u}^T \mathbf{b} d\Omega - \int_{\Gamma} \delta \mathbf{u}^T \mathbf{t} d\Gamma = 0 \quad (6)$$

where δ denotes the variational operator. \mathbf{b} represents the body force and \mathbf{t} represents the surface traction.

Considering an isotropic material with Young's modulus E and Poisson's ratio ν , the relevant material matrices can be written by

$$\mathbf{D}_m = \frac{Et}{(1-\nu^2)} \begin{bmatrix} 1 & \nu & 0 \\ \nu & 1 & 0 \\ 0 & 0 & 1-\nu/2 \end{bmatrix} \quad (7)$$

$$\mathbf{D}_b = \frac{Et^3}{12(1-\nu^2)} \begin{bmatrix} 1 & \nu & 0 \\ \nu & 1 & 0 \\ 0 & 0 & 1-\nu/2 \end{bmatrix} \quad (8)$$

$$\mathbf{D}_s = \kappa t G \begin{bmatrix} 1 & 0 \\ 0 & 1 \end{bmatrix} \quad (9)$$

where t is the thickness of the shell. G is the shear modulus and $\kappa = 5/6$ is a shear correction factor.

For free vibration problems, if the damping is not considered, the corresponding standard Galerkin weak form can be expressed as

$$\int_{\Omega} (\delta \boldsymbol{\varepsilon}_m)^T \mathbf{D}_m \boldsymbol{\varepsilon}_m d\Omega + \int_{\Omega} \delta \kappa^T \mathbf{D}_b \kappa d\Omega + \int_{\Omega} \delta \gamma^T \mathbf{D}_s \gamma d\Omega + \int_{\Omega} \delta \mathbf{u}^T \mathbf{m} \mathbf{u}'' d\Omega = 0 \quad (10)$$

where the mass matrix \mathbf{m} is defined as

$$\mathbf{m} = \text{diag}[\rho t \ \rho t \ \rho t^3/12 \ \rho t^3/12 \ 0] \quad (11)$$

in which ρ is the mass density of the material.

2.2. The general flat shell element formulation

The bounded problem domain Ω , $\Omega = \cup_{e=1}^{N_e} \Omega_e$ and $\Omega_i \cap \Omega_j = \emptyset$, $i \neq j$, is first divided into N_e finite elements. For the general case, the finite solution $\mathbf{d} = [u \ v \ w \ \theta_x \ \theta_y \ \theta_z]^T$ for the shell model can be expressed as

$$\mathbf{d} = \sum_{i=1}^{N_n} \mathbf{N}_i \mathbf{d}_i \quad (12)$$

where N_n is the total number of nodes, $\mathbf{d}_i = [u_i \ v_i \ w_i \ \theta_{xi} \ \theta_{yi} \ \theta_{zi}]^T$ is the generalized nodal displacement components in natural coordinate system for node i , \mathbf{N}_i is a diagonal matrix of linear shape functions given by

$$\mathbf{N}_i = \text{diag}[N_i(\mathbf{x}) \ N_i(\mathbf{x}) \ N_i(\mathbf{x}) \ N_i(\mathbf{x}) \ N_i(\mathbf{x}) \ N_i(\mathbf{x})] \quad (13)$$

in which $N_i(\mathbf{x})$ is the simplest linear shape function.

Substituting Eq. (13) into Eqs. (1)–(3), the linear membrane strain $\boldsymbol{\varepsilon}_m^l$, nonlinear membrane strain $\boldsymbol{\varepsilon}_m^{nl}$, curvature κ and transverse shear strain γ can be obtained in the following approximate forms

$$\begin{aligned} \boldsymbol{\varepsilon}_m^l &= \sum_{i=1}^{N_n} \mathbf{B}_{mi}^l \mathbf{d}_i \\ \boldsymbol{\varepsilon}_m^{nl} &= \sum_{i=1}^{N_n} \frac{1}{2} \mathbf{B}_{mi}^{nl} \mathbf{d}_i \\ \kappa &= \sum_{i=1}^{N_n} \mathbf{B}_{bi} \mathbf{d}_i \\ \gamma &= \sum_{i=1}^{N_n} \mathbf{B}_{si} \mathbf{d}_i \end{aligned} \quad (14)$$

where

$$\mathbf{B}_{mi}^l = \begin{bmatrix} \frac{\partial N_i}{\partial x} & 0 & 0 & 0 & 0 & 0 \\ 0 & \frac{\partial N_i}{\partial y} & 0 & 0 & 0 & 0 \\ \frac{\partial N_i}{\partial y} & \frac{\partial N_i}{\partial x} & 0 & 0 & 0 & 0 \end{bmatrix} \quad (15)$$

$$\mathbf{B}_{bi} = \begin{bmatrix} 0 & 0 & 0 & 0 & \frac{\partial N_i}{\partial x} & 0 \\ 0 & 0 & 0 & -\frac{\partial N_i}{\partial y} & 0 & 0 \\ 0 & 0 & 0 & -\frac{\partial N_i}{\partial x} & \frac{\partial N_i}{\partial y} & 0 \end{bmatrix} \quad (16)$$

$$\mathbf{B}_{si} = \begin{bmatrix} 0 & 0 & \frac{\partial N_i}{\partial x} & 0 & N_i & 0 \\ 0 & 0 & \frac{\partial N_i}{\partial y} & -N_i & 0 & 0 \end{bmatrix} \quad (17)$$

$$\mathbf{B}_{mi}^{nl} = \mathbf{A}_i \mathbf{G}_{ki} \quad (18)$$

in which

$$\mathbf{A}_i = \begin{bmatrix} \frac{\partial N_i}{\partial x} w_i & 0 & \frac{\partial N_i}{\partial y} w_i \\ 0 & \frac{\partial N_i}{\partial y} w_i & \frac{\partial N_i}{\partial x} w_i \end{bmatrix}^T \quad (19)$$

$$\mathbf{G}_i = \begin{bmatrix} 0 & 0 & \partial N_i / \partial x & 0 & 0 & 0 \\ 0 & 0 & \partial N_i / \partial y & 0 & 0 & 0 \end{bmatrix} \quad (20)$$

By means of the standard FEM formulation, the discretized system equations of the shell for static analysis can be written as:

$$\mathbf{Kd} = \mathbf{f} \quad (21)$$

where \mathbf{K} is the global stiffness matrix and

$$\mathbf{K} = \sum_{i=1}^{N_e} \int_{\Omega_i^e} (\mathbf{B}_i)^T \mathbf{D} \mathbf{B}_i d\Omega = \sum_{i=1}^{N_e} (\mathbf{K}_i^l + \mathbf{K}_i^{nl}) \quad (22)$$

where N_e is the total number of elements in the problem domain and Ω_i^e is the area for element i ; $\mathbf{D} = \text{diag}[\mathbf{D}_m \ \mathbf{D}_b \ \mathbf{D}_s]$ is the related stiffness constitutive coefficients; \mathbf{B}_i is the strain matrix; \mathbf{K}_i^l and \mathbf{K}_i^{nl} are the linear and nonlinear term of the element stiffness matrix.

$$\mathbf{B}_i = \mathbf{B}_i^l + \mathbf{B}_i^{nl} = \begin{bmatrix} \mathbf{B}_{mi}^l \\ \mathbf{B}_{bi}^l \\ \mathbf{B}_{si}^l \end{bmatrix} + \begin{bmatrix} \mathbf{B}_{mi}^{nl} \\ \mathbf{0} \\ \mathbf{0} \end{bmatrix} \quad (23)$$

$$\mathbf{K}_i^l = \mathbf{K}_{mi}^l + \mathbf{K}_{bi}^l + \mathbf{K}_{si}^l = \left[(\mathbf{B}_{mi}^l)^T \mathbf{D}_m \mathbf{B}_{mi}^l + (\mathbf{B}_{bi}^l)^T \mathbf{D}_b \mathbf{B}_{bi}^l + (\mathbf{B}_{si}^l)^T \mathbf{D}_s \mathbf{B}_{si}^l \right] A_i \quad (24)$$

$$\mathbf{K}_i^{nl} = \left[\frac{1}{2} (\mathbf{B}_i^l)^T \mathbf{D} \mathbf{B}_i^l + (\mathbf{B}_i^{nl})^T \mathbf{D} \mathbf{B}_i^l + \frac{1}{2} (\mathbf{B}_i^{nl})^T \mathbf{D} \mathbf{B}_i^{nl} \right] A_i \quad (25)$$

The global force vector can be obtained as follows:

$$\mathbf{f} = \int_{\Omega} \mathbf{N}^T \mathbf{b} d\Omega + \mathbf{f}_b = \sum_{i=1}^{N_e} \int_{\Omega_i^e} \mathbf{N}^T \mathbf{b} d\Omega + \mathbf{f}_b \quad (26)$$

in which \mathbf{f}_b relates to the prescribed boundary loads.

For free vibration analysis, the external force vector will vanish and the discretized governing equation becomes:

$$(\mathbf{K} - \omega^2 \mathbf{M}) \mathbf{d} = \mathbf{0} \quad (27)$$

where ω is the angular frequency of the free vibration.

2.3. The discrete shear gap (DSG) technique for Reissner-Mindlin shell

For the Reissner-Mindlin shell, it is known that the shear locking phenomenon often occurs when the thickness of the shell becomes small, where the pure bending action dominates the deformation. This is because the transverse shear strains do not vanish under the pure bending conditions based on the Reissner-Mindlin theory. Such a conflict of the bending and shear strain fields under thin shell situations leads to the shear locking problem. The shear locking results in an additional, artificial stiffness to the system and leads to inaccurate solutions. In order to overcome this problem, Bletzinger et al. have proposed the discrete shear gap (DSG) method to alter the shear strain field [20]. In the DSG, the shear strain is linear interpolated from the shear gaps of displacement by using the standard element shape functions and the operator matrix related to shear strain field can be obtained from the coordinates of nodes of the elements directly. Numerical results demonstrate that the DSG is free of shear locking and possesses several superior properties. The detailed formulation of DSG for three-node triangular element mesh (DSG3) will be presented in the following section.

The approximation of $\mathbf{d} = [u \ v \ w \ \theta_x \ \theta_y \ \theta_z]^T$ in a three-node triangular flat shell element based on Reissner-Mindlin theory can be written as follows:

$$\mathbf{d} = \sum_{i=1}^3 \text{diag}[N_i(\mathbf{x}) \ N_i(\mathbf{x}) \ N_i(\mathbf{x}) \ N_i(\mathbf{x}) \ N_i(\mathbf{x}) \ N_i(\mathbf{x})] \mathbf{d}_i \quad (28)$$

where \mathbf{d}_i is the “displacement” vector and \mathbf{N}_i is the linear shape function defined in natural coordinates, as shown as in Fig. 2

$$N_1 = 1 - \xi - \eta, \quad N_2 = \xi, \quad N_3 = \eta \quad (29)$$

The linear membrane strain $\boldsymbol{\epsilon}_m^l$, curvature $\boldsymbol{\kappa}$ can be obtained by

$$\boldsymbol{\epsilon}_m^l = [\mathbf{B}_{m1}^l \ \mathbf{B}_{m2}^l \ \mathbf{B}_{m3}^l] \mathbf{d}_i = \mathbf{B}_m^l \mathbf{d}_i \quad (30)$$

$$\boldsymbol{\kappa} = [\mathbf{B}_{b1} \ \mathbf{B}_{b2} \ \mathbf{B}_{b3}] \mathbf{d}_i = \mathbf{B}_b \mathbf{d}_i \quad (31)$$

where \mathbf{B}_m^l and \mathbf{B}_b contain the derivatives of the shape functions that are constant and can be written as

$$\mathbf{B}_{m1}^l = \frac{1}{2A_e} \begin{bmatrix} b-d & 0 & 0 & 0 & 0 & 0 \\ 0 & c-a & 0 & 0 & 0 & 0 \\ c-a & b-d & 0 & 0 & 0 & 0 \end{bmatrix} \quad (32)$$

$$\mathbf{B}_{m2}^l = \frac{1}{2A_e} \begin{bmatrix} d & 0 & 0 & 0 & 0 & 0 \\ 0 & -c & 0 & 0 & 0 & 0 \\ -c & d & 0 & 0 & 0 & 0 \end{bmatrix} \quad (33)$$

$$\mathbf{B}_{m3}^l = \frac{1}{2A_e} \begin{bmatrix} -b & 0 & 0 & 0 & 0 & 0 \\ 0 & a & 0 & 0 & 0 & 0 \\ a & -b & 0 & 0 & 0 & 0 \end{bmatrix} \quad (34)$$

$$\mathbf{B}_{b1} = \frac{1}{2A_e} \begin{bmatrix} 0 & 0 & 0 & 0 & b-d & 0 \\ 0 & 0 & 0 & a-c & 0 & 0 \\ 0 & 0 & 0 & d-b & c-a & 0 \end{bmatrix} \quad (35)$$

$$\mathbf{B}_{b2} = \frac{1}{2A_e} \begin{bmatrix} 0 & 0 & 0 & 0 & d & 0 \\ 0 & 0 & 0 & c & 0 & 0 \\ 0 & 0 & 0 & -d & -c & 0 \end{bmatrix} \quad (36)$$

$$\mathbf{B}_{b3} = \frac{1}{2A_e} \begin{bmatrix} 0 & 0 & 0 & 0 & -b & 0 \\ 0 & 0 & 0 & -a & 0 & 0 \\ 0 & 0 & 0 & b & a & 0 \end{bmatrix} \quad (37)$$

with $a = x_2 - x_1$, $b = y_2 - y_1$, $c = x_3 - x_1$, $d = y_3 - y_1$ and A_e is the area of the triangular element.

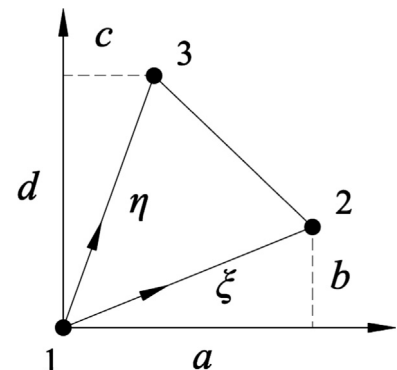


Fig. 2. The three-node triangular element and local coordinates.

In the discrete shear gap (DSG) method, the shear strains in each triangular element is given by

$$\gamma_{xz} = \sum_{i=1}^3 \frac{N_i(\mathbf{x})}{\partial x} \Delta w_{xi} + \sum_{i=1}^3 \frac{N_i(\mathbf{x})}{\partial x} \Delta w_{yi} \quad (38)$$

$$\gamma_{yz} = \sum_{i=1}^3 \frac{N_i(\mathbf{x})}{\partial y} \Delta w_{xi} + \sum_{i=1}^3 \frac{N_i(\mathbf{x})}{\partial y} \Delta w_{yi} \quad (39)$$

in which w_{xi} and w_{yi} are the discrete shear gaps at node i given by

$$\Delta w_{x1} = \Delta w_{x3} = \Delta w_{y1} = \Delta w_{y2} = 0 \quad (40)$$

$$\Delta w_{x2} = (w_2 - w_1) - \frac{1}{2}b(\theta_{x1} + \theta_{x2}) + \frac{1}{2}a(\theta_{y1} + \theta_{y2}) \quad (41)$$

$$\Delta w_{y3} = (w_3 - w_1) - \frac{1}{2}d(\theta_{x1} + \theta_{x3}) + \frac{1}{2}c(\theta_{y1} + \theta_{y3}) \quad (42)$$

Then the shear strains can be expressed as

$$\boldsymbol{\gamma} = [\mathbf{B}_{s1} \quad \mathbf{B}_{s2} \quad \mathbf{B}_{s3}] \mathbf{u}_I = \mathbf{B}_s \mathbf{d}_I \quad (43)$$

where the shear strain matrix \mathbf{B}_s is given by

$$\mathbf{B}_{s1} = \frac{1}{2A_e} \begin{bmatrix} 0 & 0 & b-d & 0 & -A_e & 0 \\ 0 & 0 & c-a & -A_e & 0 & 0 \end{bmatrix} \quad (44)$$

$$\mathbf{B}_{s2} = \frac{1}{2A_e} \begin{bmatrix} 0 & 0 & d & -\frac{bd}{2} & \frac{ad}{2} & 0 \\ 0 & 0 & -c & \frac{bc}{2} & -\frac{ac}{2} & 0 \end{bmatrix} \quad (45)$$

$$\mathbf{B}_{s1} = \frac{1}{2A_e} \begin{bmatrix} 0 & 0 & -b & \frac{bd}{2} & -\frac{bc}{2} & 0 \\ 0 & 0 & a & -\frac{ad}{2} & \frac{ac}{2} & 0 \end{bmatrix} \quad (46)$$

2.4. The treatment the drilling degree of freedom

In the previous formulation, each node in the flat shell element consists of six degrees of freedom (DOF), namely three displacement DOFs and three rotation DOFs. Actually, the third rotation degree “ θ_{zi} ”, which is the so-called drilling degree of freedom, is not necessary to construct the theoretical foundation. However, the inclusion of the third rotation degree has obvious advantages in programming and computation because both rotations and displacements at nodes can be treated in a simple manner using the coordinate transformation procedure. Unfortunately, when this six DOFs type shell element is used to solve flat shell segments or folded plate structures, a difficulty always arises if all the elements meeting at a node are co-planar. The difficulty results from the zero stiffness in the θ_{zi} direction and this always causes the singular behavior. In order to avoid the presence of this singular behavior, an arbitrary stiffness coefficient $k_{\theta_{zi}}$ is inserted at the related degree of freedom θ_{zi} in this work and the related equation can be expressed as

$$k_{\theta_{zi}} \theta_{zi} = 0 \quad (47)$$

Here the value of the arbitrary stiffness coefficient $k_{\theta_{zi}}$ is chosen to be 10^{-3} times the maximum diagonal value of the element stiffness matrix [29]. Then the stiffness matrix to node i can be obtained as

$$\mathbf{k}_i = \begin{bmatrix} [\mathbf{k}_p]_{2 \times 2} & \mathbf{0}_{2 \times 3} & 0 \\ \mathbf{0}_{3 \times 2} & [\mathbf{k}_b]_{3 \times 3} & 0 \\ 0 & 0 & 10^{-3} \max(k_{i,i}) \end{bmatrix} \quad (48)$$

in which \mathbf{k}_p and \mathbf{k}_b is the related stiffness matrix corresponding to in-plane and bending actions, respectively.

2.5. Formulation of the nonlinear problems

In this work, the modified Newton-Raphson method is used to solve the nonlinear equilibrium equation. Eq. (21) can be rewritten as

$$\mathbf{g}(\mathbf{d}) = \mathbf{K}\mathbf{d} - \mathbf{F} = \mathbf{0} \quad (49)$$

It is assumed that the external load \mathbf{F} is proportional to the fixed load \mathbf{F}_0

$$\mathbf{F} = \lambda \mathbf{F}_0 \quad (50)$$

where λ is the related proportion factor.

Then Eq. (49) can be rewritten as

$$\mathbf{g}(\mathbf{d}, \lambda) = \mathbf{K}\mathbf{d} - \lambda \mathbf{F}_0 \quad (51)$$

To obtain a new equilibrium, the displacement vector \mathbf{d} and the proportion factor λ are updated by increments. Using the Taylor series expansion, Eq. (51) can be expressed as the following incremental form:

$$\mathbf{g}(\mathbf{d} + \Delta\mathbf{d}, \lambda + \Delta\lambda) = \mathbf{g}(\mathbf{d}, \lambda) + \mathbf{K}_t \Delta\mathbf{d} - \Delta\lambda \mathbf{F}_0 = \mathbf{0} \quad (52)$$

where $\Delta\mathbf{d}$ is the displacement vector increments, $\Delta\lambda$ is the proportion factor increments and \mathbf{K}_t is the tangent stiffness matrix.

$$\mathbf{K}_t = \sum_{i=1}^{N_e} \mathbf{K}_{ti} = \sum_{i=1}^{N_e} (\mathbf{K}_i^l + \mathbf{K}_i^{nl} + \mathbf{K}_{gi}) \quad (53)$$

where \mathbf{K}_{gi} is the element geometric stiffness matrix.

$$\mathbf{K}_{gi} = \int_{\Omega_e} \mathbf{G}^T \bar{\mathbf{N}} \mathbf{G} d\Omega \quad (54)$$

in which \mathbf{G} is given in Eq. (20) and the membrane stress matrix $\bar{\mathbf{N}}$ is defined as

$$\bar{\mathbf{N}} = \begin{bmatrix} N_x & N_{xy} \\ N_{xy} & N_y \end{bmatrix} \quad (55)$$

where N_x , N_y and N_{xy} are the components of membrane force vector given in Eq. (5).

In the process of solving the nonlinear equation, each load step includes the application of external load and subsequent iterations to obtain equilibrium. The generalized equation for the incremental-iterative process is given by

$$[\mathbf{K}_t]_i \Delta \mathbf{d}_i^j = \Delta \lambda_i^j \mathbf{F}_0 - \mathbf{g}_i^{j-1} = \Delta \lambda_i^j \mathbf{F}_0 - [\mathbf{K}(\mathbf{d}_i^{j-1}) \mathbf{d}_i - \Delta \lambda_i^{j-1} \mathbf{F}_0] \quad (56)$$

where the subscript i is the load step number and the superscript j is the iteration cycle.

Then the incremental displacement vector can be expressed as

$$\begin{aligned} \Delta \mathbf{d}_i^j &= ([\mathbf{K}_t]_i)^{-1} \{ \Delta \lambda_i^j \mathbf{F}_0 - [\mathbf{K}(\mathbf{d}_i^{j-1}) \mathbf{d}_i - \Delta \lambda_i^{j-1} \mathbf{F}_0] \} \\ &= \Delta \lambda_i^j [\mathbf{d}_f]_i + [\Delta \mathbf{d}_r]_i^j \end{aligned} \quad (57)$$

From Eq. (57), it is seen that the incremental displacement vector $\Delta \mathbf{d}_i^j$ can be split into two parts. The first part in Eq. (57) is from external load increment and the second part is from the residual force.

In this work, the arc-length method is used to determine the load increment and the convergence criterion is given by

$$\frac{\|\mathbf{g}(\mathbf{d}, \lambda)\|}{\|\mathbf{F}(\mathbf{d}, \lambda)\|} < \zeta \quad (58)$$

where ζ is the tolerance for convergence constant and it is set to 0.0001 in this paper.

3. The detailed formulation of S α -DSG3 for shells

3.1. The construction of node-based smoothed strain field

In the S α -DSG3 model, the node-based smoothed strain field, which consists of the information from the adjacent elements, is utilized to reconstruct a novel linear strain field. Therefore, the detailed formulation of node-based smoothed strain field for shells are given in this sub-section.

As shown in Fig. 3, the original problem domain Ω is first divided into N_e elements with N_n nodes using triangular mesh, such that $\Omega = \sum_{i=1}^{N_e} \Omega_i^e$, and $\Omega_i^e \cap \Omega_j^e = \emptyset$, $i \neq j$, as in the standard FEM. In order to perform the node-based strain smoothing operations, the problem domain is further divided into N_n smoothing domains, such that $\Omega = \sum_{k=1}^{N_n} \Omega_k^s$ and $\Omega_i^s \cap \Omega_j^s = \emptyset$, $i \neq j$. These smoothing domains, which are associated with the field nodes, are created by sequentially connecting the mid-edge-point to the centers of surrounding elements. After obtaining the above-mentioned smoothing domains, the smoothed strains on the smoothing domain Ω_k^s can be obtained by

$$\begin{aligned}\bar{\boldsymbol{\varepsilon}}_m^l(\mathbf{x}) &= \frac{1}{A_k^s} \int_{\Omega_k^s} \boldsymbol{\varepsilon}_m^l(\mathbf{x}) d\Omega \\ \bar{\boldsymbol{\varepsilon}}_m^{nl}(\mathbf{x}) &= \frac{1}{A_k^s} \int_{\Omega_k^s} \boldsymbol{\varepsilon}_m^{nl}(\mathbf{x}) d\Omega \\ \bar{\mathbf{k}}(\mathbf{x}) &= \frac{1}{A_k^s} \int_{\Omega_k^s} \mathbf{k}(\mathbf{x}) d\Omega \\ \bar{\gamma}(\mathbf{x}) &= \frac{1}{A_k^s} \int_{\Omega_k^s} \gamma(\mathbf{x}) d\Omega\end{aligned}\quad (59)$$

where $\boldsymbol{\varepsilon}_m^l(\mathbf{x})$, $\boldsymbol{\varepsilon}_m^{nl}(\mathbf{x})$, $\mathbf{k}(\mathbf{x})$ and $\gamma(\mathbf{x})$ are the compatible strains from the standard FEM and A_k^s is the area of the smoothing domain Ω_k^s .

For shell structures, the transformation from a common global coordinate (which is denoted by $x - y - z$) to local coordinate system (which is denoted by $\hat{x} - \hat{y} - \hat{z}$) is needed. The local coordinate system is defined as follows: as shown in Fig. 4, let \hat{x} directions be directly along the side 1–2 of the triangular element, then the \hat{z} direction which must be normal to the plane of the element can be defined through a “vector” cross product of two sides of the triangle, finally the \hat{y} is then defined as the cross product of the unit vectors in the \hat{x} direction and \hat{z} direction.

Once the local coordinate system for each element is defined, the corresponding compatible strains based on this local coordinate system can be obtained. In order to perform the strain

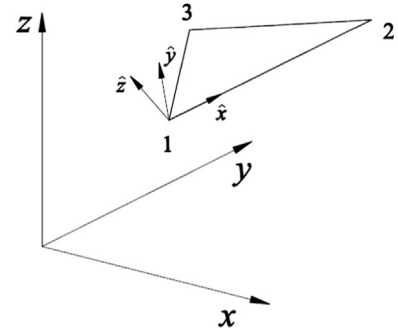


Fig. 4. The local and global coordinates for a triangular element.

smoothing operations in the same local coordinate system for each smoothing domain, the node local coordinate system $\hat{x} - \hat{y} - \hat{z}$ is defined here. For the convenience of computation, this coordinate system is exactly the same local coordinate system defined in the first sub-domain, as shown in Fig. 5. Through the transformation rules for each element, the compatible strains in each sub-domain based on the node coordinate system can be obtained by

$$\begin{aligned}\boldsymbol{\varepsilon}_m^l(\mathbf{x}) &= \mathbf{R}_{m1} \mathbf{R}_{m2} \hat{\boldsymbol{\varepsilon}}_m^l(\mathbf{x}) = \mathbf{R}_{m1} \mathbf{R}_{m2} \mathbf{B}_m^l \mathbf{T} \mathbf{d}_l \\ \boldsymbol{\varepsilon}_m^{nl}(\mathbf{x}) &= \mathbf{R}_{m1} \mathbf{R}_{m2} \hat{\boldsymbol{\varepsilon}}_m^{nl}(\mathbf{x}) = \mathbf{R}_{m1} \mathbf{R}_{m2} \mathbf{B}_m^{nl} \mathbf{T} \mathbf{d}_l \\ \mathbf{k}(\mathbf{x}) &= \mathbf{R}_{b1} \mathbf{R}_{b2} \hat{\mathbf{k}}(\mathbf{x}) = \mathbf{R}_{b1} \mathbf{R}_{b2} \mathbf{B}_b \mathbf{T} \mathbf{d}_l \\ \gamma(\mathbf{x}) &= \mathbf{R}_{s1} \mathbf{R}_{s2} \hat{\gamma}(\mathbf{x}) = \mathbf{R}_{s1} \mathbf{R}_{s2} \mathbf{B}_s \mathbf{T} \mathbf{d}_l\end{aligned}\quad (60)$$

in which $\hat{\boldsymbol{\varepsilon}}_m^l(\mathbf{x})$, $\hat{\mathbf{k}}(\mathbf{x})$ and $\hat{\gamma}(\mathbf{x})$ are strains in element local coordinate system, \mathbf{T} is the transformation matrix from global coordinate system $x - y - z$ to element coordinate system $\hat{x} - \hat{y} - \hat{z}$ and

$$\mathbf{T} = \begin{bmatrix} \Lambda & \mathbf{0} \\ \mathbf{0} & \Lambda \end{bmatrix} \quad (61)$$

in which

$$\Lambda = \begin{bmatrix} \cos(\hat{x}, x) & \cos(\hat{x}, y) & \cos(\hat{x}, z) \\ \cos(\hat{y}, x) & \cos(\hat{y}, y) & \cos(\hat{y}, z) \\ \cos(\hat{z}, x) & \cos(\hat{z}, y) & \cos(\hat{z}, z) \end{bmatrix} = \begin{bmatrix} c_{\hat{x}x} & c_{\hat{x}y} & c_{\hat{x}z} \\ c_{\hat{y}x} & c_{\hat{y}y} & c_{\hat{y}z} \\ c_{\hat{z}x} & c_{\hat{z}y} & c_{\hat{z}z} \end{bmatrix} \quad (62)$$

$$\mathbf{R}_{m1} = \mathbf{R}_{b1} = \begin{bmatrix} c_{\hat{x}x}^2 & c_{\hat{x}y}^2 & c_{\hat{x}z}^2 & c_{\hat{x}x} c_{\hat{x}y} & c_{\hat{x}y} c_{\hat{x}z} & c_{\hat{x}x} c_{\hat{x}z} \\ c_{\hat{y}x}^2 & c_{\hat{y}y}^2 & c_{\hat{y}z}^2 & c_{\hat{y}x} c_{\hat{y}y} & c_{\hat{y}y} c_{\hat{y}z} & c_{\hat{y}x} c_{\hat{y}z} \\ 2c_{\hat{x}x} c_{\hat{y}x} & 2c_{\hat{x}y} c_{\hat{y}x} & 2c_{\hat{x}z} c_{\hat{y}x} & c_{\hat{x}x} c_{\hat{y}y} + c_{\hat{y}x} c_{\hat{x}y} & c_{\hat{x}z} c_{\hat{y}y} + c_{\hat{y}z} c_{\hat{x}y} & c_{\hat{x}x} c_{\hat{y}z} + c_{\hat{y}x} c_{\hat{x}z} \end{bmatrix} \quad (63)$$

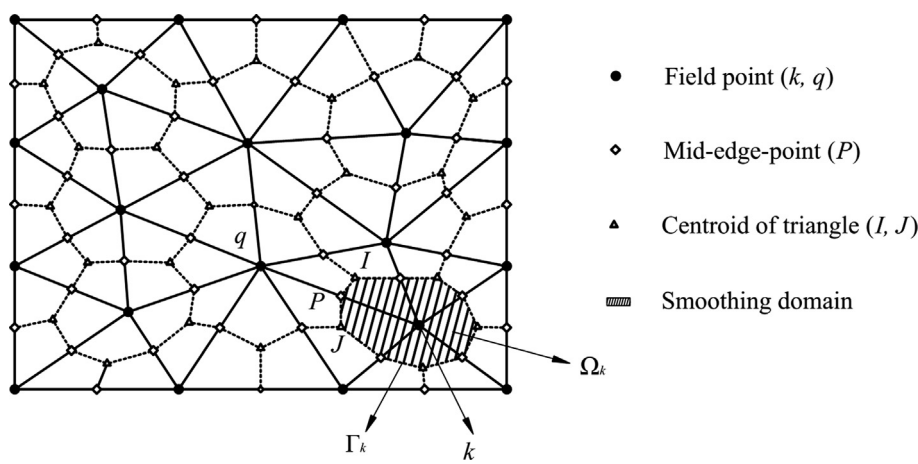


Fig. 3. The node-based smoothing domains in triangular meshes.

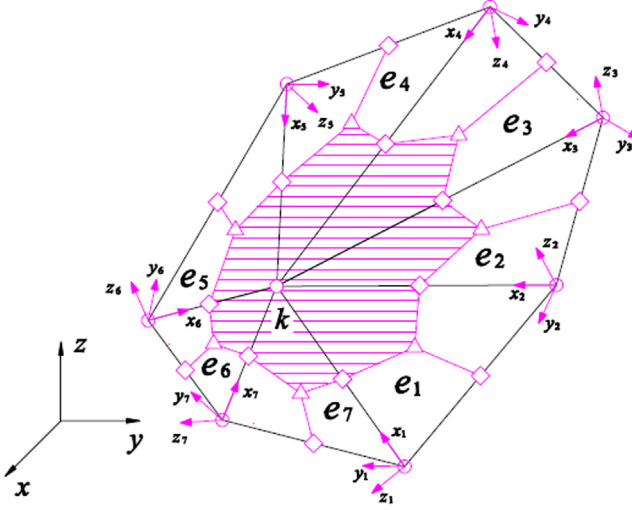


Fig. 5. The triangular flat shell element for node-based strain smoothing technique.

$$\mathbf{R}_{s1} = \begin{bmatrix} 2c_{\hat{x}\hat{x}}c_{\hat{z}\hat{x}} & 2c_{\hat{x}\hat{y}}c_{\hat{z}\hat{y}} & 2c_{\hat{x}\hat{z}}c_{\hat{z}\hat{z}} & c_{\hat{x}\hat{x}}c_{\hat{z}\hat{y}} + c_{\hat{z}\hat{x}}c_{\hat{x}\hat{y}} & c_{\hat{x}\hat{x}}c_{\hat{z}\hat{y}} + c_{\hat{z}\hat{z}}c_{\hat{x}\hat{y}} & c_{\hat{x}\hat{x}}c_{\hat{z}\hat{z}} + c_{\hat{z}\hat{x}}c_{\hat{x}\hat{z}} \\ 2c_{\hat{y}\hat{x}}c_{\hat{z}\hat{x}} & 2c_{\hat{y}\hat{y}}c_{\hat{z}\hat{y}} & 2c_{\hat{y}\hat{z}}c_{\hat{z}\hat{z}} & c_{\hat{y}\hat{x}}c_{\hat{z}\hat{y}} + c_{\hat{z}\hat{y}}c_{\hat{x}\hat{y}} & c_{\hat{y}\hat{x}}c_{\hat{z}\hat{y}} + c_{\hat{z}\hat{z}}c_{\hat{y}\hat{y}} & c_{\hat{y}\hat{x}}c_{\hat{z}\hat{z}} + c_{\hat{z}\hat{x}}c_{\hat{y}\hat{z}} \end{bmatrix} \quad (64)$$

$$\mathbf{R}_{m2} = \mathbf{R}_{b2} = \begin{bmatrix} c_{\hat{x}\hat{x}}^2 & c_{\hat{y}\hat{x}}^2 & c_{\hat{x}\hat{x}}c_{\hat{y}\hat{x}} \\ c_{\hat{x}\hat{y}}^2 & c_{\hat{y}\hat{y}}^2 & c_{\hat{x}\hat{y}}c_{\hat{y}\hat{y}} \\ c_{\hat{x}\hat{z}}^2 & c_{\hat{y}\hat{z}}^2 & c_{\hat{x}\hat{z}}c_{\hat{y}\hat{z}} \\ 2c_{\hat{x}\hat{x}}c_{\hat{x}\hat{y}} & 2c_{\hat{y}\hat{x}}c_{\hat{y}\hat{y}} & c_{\hat{x}\hat{x}}c_{\hat{y}\hat{y}} + c_{\hat{y}\hat{x}}c_{\hat{y}\hat{x}} \\ 2c_{\hat{x}\hat{y}}c_{\hat{x}\hat{z}} & 2c_{\hat{y}\hat{y}}c_{\hat{y}\hat{z}} & c_{\hat{x}\hat{y}}c_{\hat{y}\hat{z}} + c_{\hat{x}\hat{z}}c_{\hat{y}\hat{y}} \\ 2c_{\hat{x}\hat{x}}c_{\hat{x}\hat{z}} & 2c_{\hat{y}\hat{x}}c_{\hat{y}\hat{z}} & c_{\hat{x}\hat{x}}c_{\hat{y}\hat{z}} + c_{\hat{x}\hat{z}}c_{\hat{y}\hat{x}} \end{bmatrix} \quad (65)$$

$$\mathbf{R}_{s2} = \begin{bmatrix} c_{\hat{x}\hat{x}}c_{\hat{z}\hat{x}} & c_{\hat{y}\hat{x}}c_{\hat{z}\hat{x}} \\ c_{\hat{x}\hat{y}}c_{\hat{z}\hat{y}} & c_{\hat{y}\hat{y}}c_{\hat{z}\hat{y}} \\ c_{\hat{x}\hat{z}}c_{\hat{z}\hat{z}} & c_{\hat{y}\hat{z}}c_{\hat{z}\hat{z}} \\ c_{\hat{x}\hat{x}}c_{\hat{z}\hat{y}} + c_{\hat{x}\hat{y}}c_{\hat{z}\hat{x}} & c_{\hat{y}\hat{x}}c_{\hat{z}\hat{y}} + c_{\hat{y}\hat{y}}c_{\hat{z}\hat{x}} \\ c_{\hat{x}\hat{z}}c_{\hat{z}\hat{y}} + c_{\hat{x}\hat{y}}c_{\hat{z}\hat{z}} & c_{\hat{y}\hat{z}}c_{\hat{z}\hat{y}} + c_{\hat{y}\hat{y}}c_{\hat{z}\hat{z}} \\ c_{\hat{x}\hat{x}}c_{\hat{z}\hat{z}} + c_{\hat{x}\hat{z}}c_{\hat{z}\hat{x}} & c_{\hat{y}\hat{x}}c_{\hat{z}\hat{z}} + c_{\hat{y}\hat{z}}c_{\hat{z}\hat{x}} \end{bmatrix} \quad (66)$$

where $\cos(\hat{x}, x)$ is the cosine of the angle between the \hat{x} axis and the x axis, and so on.

Substituting Eq. (60) into Eq. (59), the node-based smoothed strain field can be obtained by

$$\begin{aligned} \bar{\boldsymbol{\epsilon}}_m^l(\mathbf{x}) &= \frac{1}{A_k^s} \int_{\Omega_k^s} \mathbf{R}_{m1} \mathbf{R}_{m2} \hat{\boldsymbol{\epsilon}}_m^l(\mathbf{x}) d\Omega \\ \bar{\boldsymbol{\epsilon}}_m^{nl}(\mathbf{x}) &= \frac{1}{A_k^s} \int_{\Omega_k^s} \mathbf{R}_{m1} \mathbf{R}_{m2} \hat{\boldsymbol{\epsilon}}_m^{nl}(\mathbf{x}) d\Omega \\ \bar{\mathbf{k}}_k(\mathbf{x}) &= \frac{1}{A_k^s} \int_{\Omega_k^s} \mathbf{R}_{b1} \mathbf{R}_{b2} \hat{\mathbf{k}}(\mathbf{x}) d\Omega \\ \bar{\gamma}_k(\mathbf{x}) &= \frac{1}{A_k^s} \int_{\Omega_k^s} \mathbf{R}_{s1} \mathbf{R}_{s2} \hat{\gamma}(\mathbf{x}) d\Omega \end{aligned} \quad (67)$$

3.2. The construction of a novel linear strain field

In this sub-section, the detailed process of constructing a novel linear strain field is presented. For the convenience of notation, the strain components (the membrane strain $\boldsymbol{\epsilon}_m$, the curvatures \mathbf{k} and the transverse shear strain γ) are denoted by $\boldsymbol{\epsilon}$ and the corresponding constitutive matrices (\mathbf{D}_m , \mathbf{D}_b , \mathbf{D}_s) are denoted by \mathbf{D} . Actually, the assumed liner strain field is constructed by combining the node-based smoothed strain in the last section and the compatible

strain from the standard FEM with a particular elegant procedure. As shown in Fig. 6, the smoothing domain for node k consists of M sub-domains, in each sub-domain $\Omega_{k,i}$, the strain $\boldsymbol{\epsilon}_P$, $\boldsymbol{\epsilon}_I$ at mid-edge-point P , I are defined by

$$\begin{aligned} \boldsymbol{\epsilon}_P = \boldsymbol{\epsilon}_I &= \boldsymbol{\epsilon}_{k,i} - \frac{\alpha\sqrt{6}}{3}(\bar{\boldsymbol{\epsilon}}_k - \boldsymbol{\epsilon}_{k,i}) \\ \bar{\boldsymbol{\epsilon}}_k &= \alpha\sqrt{6}\bar{\boldsymbol{\epsilon}}_k + (1 - \alpha\sqrt{6})\boldsymbol{\epsilon}_{k,i} - \frac{\alpha\sqrt{6}}{3}(\bar{\boldsymbol{\epsilon}}_k - \boldsymbol{\epsilon}_{k,i}), \quad \forall \alpha \in \mathbb{R} \end{aligned} \quad (68)$$

where α is a variable parameter, $\boldsymbol{\epsilon}_{k,i}$ is the compatible strains obtained from standard FEM and $\bar{\boldsymbol{\epsilon}}_k$ is the node-based smoothed strain obtained from NS-FEM.

The strain field in the sub-domain $\Omega_{k,i}$ can be reconstructed by

$$\bar{\boldsymbol{\epsilon}}(\mathbf{x}) = L_1(\mathbf{x})\boldsymbol{\epsilon}_k + L_2(\mathbf{x})\boldsymbol{\epsilon}_P + L_3(\mathbf{x})\boldsymbol{\epsilon}_I \quad (69)$$

in which $L_1(\mathbf{x})$, $L_2(\mathbf{x})$ and $L_3(\mathbf{x})$ denote the area coordinates for sub-triangular domain $\Omega_{k,i}$.

Substituting Eq. (68) into Eq. (69) and using the following formula

$$L_1(\mathbf{x}) + L_2(\mathbf{x}) + L_3(\mathbf{x}) = 1 \quad (70)$$

Then Eq. (69) can be simplified by

$$\bar{\boldsymbol{\epsilon}}(\mathbf{x}) = \boldsymbol{\epsilon}_{k,i} + \alpha\sqrt{6}(\bar{\boldsymbol{\epsilon}}_k - \boldsymbol{\epsilon}_{k,i})\left(L_1(\mathbf{x}) - \frac{1}{3}\right) = \boldsymbol{\epsilon}_{k,i} + \alpha\boldsymbol{\epsilon}_{k,i}^{\text{add}}(\mathbf{x}) \quad (71)$$

in which $\boldsymbol{\epsilon}_{k,i}^{\text{add}}(\mathbf{x})$ is an additional strain and it is a linear function in sub-triangular domain $\Omega_{k,i}$.

In this way, a novel linear strain field with a parameter α is constructed. Using the following equation

$$\int_{\Omega_{k,i}} L_1^p L_2^q L_3^r = \frac{p!q!r!}{(p+q+r+2)!} 2A_{k,i} \quad (72)$$

It is clear that

$$\int_{\Omega_{k,i}} \boldsymbol{\epsilon}_{k,i}^{\text{add}}(\mathbf{x}) d\Omega = \sqrt{6}(\bar{\boldsymbol{\epsilon}}_k - \boldsymbol{\epsilon}_{k,i}) \int_{\Omega_{k,i}} \left(L_1(\mathbf{x}) - \frac{1}{3}\right) d\Omega = 0 \quad (73)$$

From Eq. (73), it obvious that the zero-sum property, which is similar to the orthogonal condition used in the stabilization formulation, is satisfied.

Performing the integration over the entire problem domain and using the zero-sum property given in Eq. (73), we have

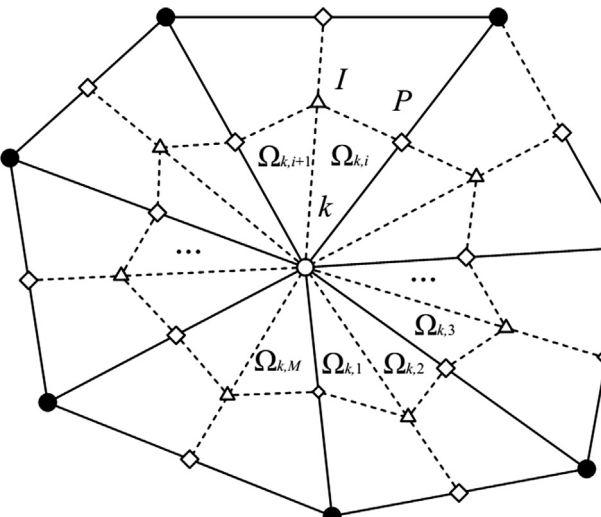


Fig. 6. The node-based smoothing domain and triangular sub-domains associated with node k .

$$\int_{\Omega} \boldsymbol{\epsilon}^{\text{add}}(\mathbf{x}) d\Omega = \sum_{k=1}^{N_n} \sum_{i=1}^M \int_{\Omega_{k,i}} \boldsymbol{\epsilon}_{k,i}^{\text{add}}(\mathbf{x}) d\Omega = \mathbf{0} \quad (74)$$

Then the following equation is obtained

$$\int_{\Omega} \bar{\boldsymbol{\epsilon}} d\Omega = \int_{\Omega} \boldsymbol{\epsilon}_{k,i} d\Omega + \int_{\Omega} \boldsymbol{\epsilon}_{k,i}^{\text{add}}(\mathbf{x}) d\Omega = \sum_{k=1}^{N_n} \sum_{i=1}^M \int_{\Omega_{k,i}} \boldsymbol{\epsilon}_{k,i} d\Omega \quad (75)$$

It is clear that the constructed linear strain field is legal and the additional strain term $\boldsymbol{\epsilon}_{k,i}^{\text{add}}$ has no extra effect on the constant stress state which is essential in the standard patch test. Based on the above formulation, a novel linear strain field with a parameter α is obtained. It is reasonable that this linear strain field is more effective to describe the exact strain field than the original piecewise constant strain field. In addition, by changing the value of the parameter α , a proper softened stiffness matrix can be obtained and the desired solution can be achieved.

3.3. Weak form formulation for the reconstructed linear strain field

In this paper, we use the Galerkin-like weakform [5,43,44], which can be derived from the modified Hellinger-Reissner variational principle, to construct a novel super-convergent shell element. In this Galerkin-like weakform. Based on the Hellinger-Reissner variational principle, the energy functional can be obtained by

$$\Pi_{HR} = -\frac{1}{2} \int_{\Omega} (\bar{\boldsymbol{\epsilon}})^T \mathbf{D} \bar{\boldsymbol{\epsilon}} d\Omega + \int_{\Omega} (\bar{\boldsymbol{\epsilon}})^T \mathbf{D} \boldsymbol{\epsilon} d\Omega - \int_{\Omega} \mathbf{d}^T \mathbf{b} d\Omega - \int_{\Omega} \mathbf{d}^T \mathbf{t} d\Gamma \quad (76)$$

in which the strain energy is defined by

$$E = -\frac{1}{2} \int_{\Omega} (\bar{\boldsymbol{\epsilon}})^T \mathbf{D} \bar{\boldsymbol{\epsilon}} d\Omega + \int_{\Omega} (\bar{\boldsymbol{\epsilon}})^T \mathbf{D} \boldsymbol{\epsilon} d\Omega \quad (77)$$

Substituting Eq. (71) into Eq. (77) and using the zero-sum property given in Eq. (73), the total strain energy over the entire problem domain can be obtained by

$$\begin{aligned} E &= \sum_{k=1}^{N_n} \sum_{i=1}^M \left[-\frac{1}{2} \int_{\Omega_{k,i}} (\bar{\boldsymbol{\epsilon}})^T \mathbf{D} \bar{\boldsymbol{\epsilon}} d\Omega + \int_{\Omega_{k,i}} (\bar{\boldsymbol{\epsilon}})^T \mathbf{D} \boldsymbol{\epsilon}_{k,i} d\Omega \right] \\ &= \sum_{k=1}^{N_n} \sum_{i=1}^M \left[-\frac{1}{2} \int_{\Omega_{k,i}} (\boldsymbol{\epsilon}_{k,i} + \alpha \boldsymbol{\epsilon}_{k,i}^{\text{add}})^T \mathbf{D} (\boldsymbol{\epsilon}_{k,i} + \alpha \boldsymbol{\epsilon}_{k,i}^{\text{add}}) d\Omega + \int_{\Omega_{k,i}} (\boldsymbol{\epsilon}_{k,i} + \alpha \boldsymbol{\epsilon}_{k,i}^{\text{add}})^T \mathbf{D} \boldsymbol{\epsilon}_{k,i} d\Omega \right] \\ &= \sum_{k=1}^{N_n} \sum_{i=1}^M \left[-\frac{1}{2} \int_{\Omega_{k,i}} \boldsymbol{\epsilon}_{k,i}^T \mathbf{D} \boldsymbol{\epsilon}_{k,i} d\Omega - \frac{1}{2} \alpha^2 \int_{\Omega_{k,i}} (\boldsymbol{\epsilon}_{k,i}^{\text{add}})^T \mathbf{D} \boldsymbol{\epsilon}_{k,i}^{\text{add}} d\Omega + \int_{\Omega_{k,i}} \boldsymbol{\epsilon}_{k,i}^T \mathbf{D} \boldsymbol{\epsilon}_{k,i} d\Omega \right] \\ &+ \sum_{k=1}^{N_n} \sum_{i=1}^M \left[-\frac{1}{2} \alpha \int_{\Omega_{k,i}} \boldsymbol{\epsilon}_{k,i}^T \mathbf{D} \boldsymbol{\epsilon}_{k,i}^{\text{add}} d\Omega - \frac{1}{2} \alpha \int_{\Omega_{k,i}} (\boldsymbol{\epsilon}_{k,i}^{\text{add}})^T \mathbf{D} \boldsymbol{\epsilon}_{k,i} d\Omega + \alpha \int_{\Omega_{k,i}} (\boldsymbol{\epsilon}_{k,i}^{\text{add}})^T \mathbf{D} \boldsymbol{\epsilon}_{k,i} d\Omega \right] \\ &= \sum_{k=1}^{N_n} \sum_{i=1}^M \left[\frac{1}{2} \int_{\Omega_{k,i}} \boldsymbol{\epsilon}_{k,i}^T \mathbf{D} \boldsymbol{\epsilon}_{k,i} d\Omega - \frac{1}{2} \alpha^2 \int_{\Omega_{k,i}} (\boldsymbol{\epsilon}_{k,i}^{\text{add}})^T \mathbf{D} \boldsymbol{\epsilon}_{k,i}^{\text{add}} d\Omega \right] \end{aligned} \quad (78)$$

Then the energy functional over the entire problem domain can be rewritten by

$$\begin{aligned} \Pi_{HR} &= \sum_{k=1}^{N_n} \sum_{i=1}^M \left[\frac{1}{2} \int_{\Omega_{k,i}} \boldsymbol{\epsilon}_{k,i}^T \mathbf{D} \boldsymbol{\epsilon}_{k,i} d\Omega - \frac{1}{2} \alpha^2 \int_{\Omega_{k,i}} (\boldsymbol{\epsilon}_{k,i}^{\text{add}})^T \mathbf{D} \boldsymbol{\epsilon}_{k,i}^{\text{add}} d\Omega \right] \\ &\quad - \int_{\Omega} \mathbf{d}^T \mathbf{b} d\Omega - \int_{\Omega} \mathbf{d}^T \mathbf{t} d\Gamma \end{aligned} \quad (79)$$

Taking a variation with respect to \mathbf{d} , we obtain

$$\begin{aligned} \Pi_{HR} &= \sum_{k=1}^{N_n} \sum_{i=1}^M \left[\frac{1}{2} \int_{\Omega_{k,i}} \delta \boldsymbol{\epsilon}_{k,i}^T \mathbf{D} \boldsymbol{\epsilon}_{k,i} d\Omega - \frac{1}{2} \alpha^2 \int_{\Omega_{k,i}} (\delta \boldsymbol{\epsilon}_{k,i}^{\text{add}})^T \mathbf{D} \boldsymbol{\epsilon}_{k,i}^{\text{add}} d\Omega \right] \\ &\quad - \int_{\Omega} \delta \mathbf{d}^T \mathbf{b} d\Omega - \int_{\Omega} \delta \mathbf{d}^T \mathbf{t} d\Gamma \end{aligned} \quad (80)$$

Eq. (80) is the Galerkin-like weak form given originally in Refs. [5,43,44] for solids. Here we use it for the reconstructed linear strain field and it can be directly used to establish the discretized

system equations for shells. From Eq. (80), it can be seen that the new Galerkin-like weak form possesses almost all the good properties in the standard Galerkin weak form. In addition, an adjustable factor α is equipped in the weak form and the proportion of the smoothed strains and the standard compatible strains in the constructed strain field can be regularized by changing the value of α . In particular, when $\alpha = 0$, the new Galerkin-like weak form is exactly the same with the standard one.

Substituting Eq. (12) into Eq. (80), the discretized governing equations can be obtained by

$$\bar{\mathbf{K}}^{\text{Sx-DSG3}} \mathbf{d} = \mathbf{F} \quad (81)$$

in which $\bar{\mathbf{K}}^{\text{Sx-DSG3}}$ denotes the system stiffness matrix given by

$$\begin{aligned} \bar{\mathbf{K}}^{\text{Sx-DSG3}} &= \sum_{k=1}^{N_n} \sum_{i=1}^M \int_{\Omega_{k,i}} \mathbf{B}_{k,i}^T \mathbf{D} \mathbf{B}_{k,i} d\Omega - \sum_{k=1}^{N_n} \sum_{i=1}^M \int_{\Omega_{k,i}} (\mathbf{B}_{k,i}^{\text{ad}})^T \mathbf{D} \mathbf{B}_{k,i}^{\text{ad}} d\Omega \\ &= \mathbf{K}^{\text{DSG3}} - \alpha^2 \mathbf{K}_{\text{ad}}^{\text{Sx-DSG3}} \end{aligned} \quad (82)$$

in which \mathbf{K}^{DSG3} is the system stiffness matrix from standard FEM and $\mathbf{K}_{\text{ad}}^{\text{Sx-DSG3}}$ is the correction stiffness matrix from the correction strain. Using Eq. (73), $\mathbf{K}_{\text{ad}}^{\text{Sx-DSG3}}$ can be expressed by

$$\begin{aligned} \mathbf{K}_{\text{ad}}^{\text{Sx-DSG3}} &= \sum_{k=1}^{N_n} \sum_{i=1}^M \int_{\Omega_{k,i}} (\mathbf{B}_{k,i}^{\text{ad}})^T \mathbf{D} \mathbf{B}_{k,i}^{\text{ad}} d\Omega \\ &= 6 \sum_{k=1}^{N_n} \sum_{i=1}^M \int_{\Omega_{k,i}} (\bar{\mathbf{B}}_k - \mathbf{B}_{k,i})^T \mathbf{D} (\bar{\mathbf{B}}_k - \mathbf{B}_{k,i}) \int_{\Omega_{k,i}} \left(L_1(\mathbf{x}) - \frac{1}{3} \right)^2 d\Omega \\ &= \frac{1}{3} \sum_{k=1}^{N_n} \sum_{i=1}^M \int_{\Omega_{k,i}} (\bar{\mathbf{B}}_k - \mathbf{B}_{k,i})^T \mathbf{D} (\bar{\mathbf{B}}_k - \mathbf{B}_{k,i}) A_{k,i} \end{aligned} \quad (83)$$

where

$$\mathbf{B}_{k,i}^{\text{ad}} = \sqrt{6} (\bar{\mathbf{B}}_k - \mathbf{B}_{k,i}) \left(L_1(\mathbf{x}) - \frac{1}{3} \right) \quad (84)$$

in which $\bar{\mathbf{B}}_k$, which is from NS-FEM, denotes the smoothed strain displacement matrix for smoothing domain Ω_k^s and $\mathbf{B}_{k,i}$, which is from standard FEM, is the standard strain displacement matrix for sub-triangular domain $\Omega_{k,i}^s$.

$$\bar{\mathbf{B}}_k = \frac{1}{A_k} \sum_{i=1}^M \int_{\Omega_{k,i}} \mathbf{B}_{k,i} d\Omega = \frac{1}{A_k} \sum_{i=1}^M \mathbf{B}_{k,i} A_{k,i} \quad (85)$$

3.4. Determination of α_{pre} for a good superconvergent solution

As mentioned in Ref. [55], it is definite that the exact solution can be obtained when an exact α (α_{exact}) is used. However, it is known that the α_{exact} is usually not easy to obtain because such a α is not only problem-dependent but also mesh-dependent. Fortunately, intensive numerical examples show that α_{exact} is approximately a linear function of the average mesh size h for a given problem. Based on this assumption, α_{exact} can be evaluated by the following equation

$$\alpha_{\text{exact}} \approx \alpha_{\text{pre}}(h) = \beta h + \gamma \quad (86)$$

in which β and γ are unknown constants which are associated with the given problem.

Following the steps below, a preferable α (α_{pre}), which is very close to α_{exact} , can be obtained.

- For a given problem, the problem domain Ω is discretized into three sets of mesh (Mesh 1, Mesh 2 and Mesh3) with the same aspect ratio. Among them, Mesh 2 is slightly finer than Mesh 1

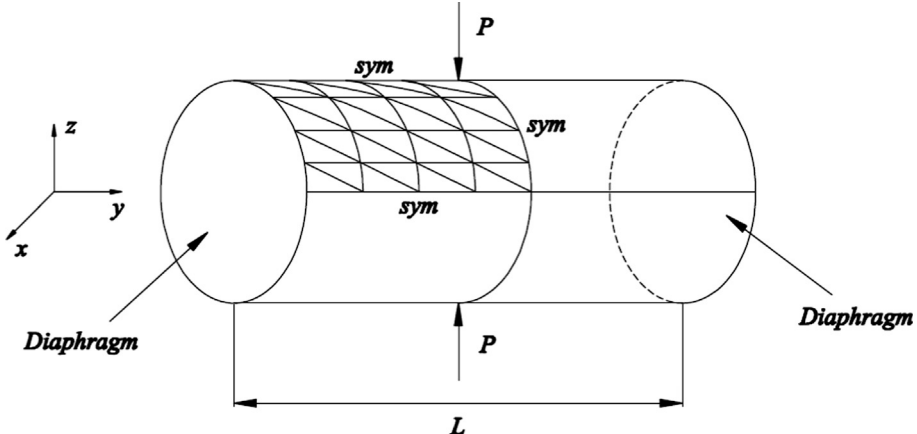


Fig. 7. The pinched cylinder with point load at the center of the surface.

Table 1

Numerical results of the normalized displacements for the cylindrical shell.

Methods	Mesh					
	4 × 4	8 × 8	12 × 12	16 × 16	20 × 20	24 × 24
S α -DSG3 ($\alpha_{\text{pre}} = 0.0278h + 1.2913$)	0.515	0.808	0.907	0.957	0.979	0.992
S α -DSG3 ($\alpha = 1.8$)	1.357	1.140	1.061	1.041	1.031	1.026
S α -DSG3 ($\alpha = 1.2$)	0.433	0.749	0.876	0.934	0.963	0.982
MITC4	0.368	0.736	0.866	0.920	0.948	0.964
MIST1	0.471	0.802	0.907	0.948	0.968	0.979
MIST2	0.438	0.780	0.894	0.939	0.962	0.975
MIST4	0.384	0.748	0.874	0.926	0.952	0.967
ES-DSG3	0.365	0.765	0.883	0.933	0.965	0.987
NS-DSG3	1.427	1.174	1.077	1.046	1.034	1.027
DSG3	0.277	0.648	0.802	0.875	0.915	0.939

Table 2

Numerical results of the strain energy for the cylindrical shell.

Methods	Mesh					
	4 × 4	8 × 8	12 × 12	16 × 16	20 × 20	24 × 24
S α -DSG3 ($\alpha_{\text{pre}} = 0.0278h + 1.2913$)	1.187E-06	1.861E-06	2.090E-06	2.204E-06	2.256E-06	2.284E-06
S α -DSG3 ($\alpha = 1.8$)	3.125E-06	2.584E-06	2.444E-06	2.398E-06	2.377E-06	2.363E-06
S α -DSG3 ($\alpha = 1.2$)	9.969E-07	1.730E-06	2.017E-06	2.151E-06	2.215E-06	2.261E-06
MITC4	8.468E-07	1.696E-06	1.994E-06	2.120E-06	2.184E-06	2.221E-06
MIST1	1.084E-06	1.846E-06	2.089E-06	2.184E-06	2.230E-06	2.256E-06
MIST2	1.008E-06	1.797E-06	2.058E-06	2.163E-06	2.215E-06	2.244E-06
MIST4	8.839E-07	1.723E-06	2.012E-06	2.132E-06	2.193E-06	2.228E-06
ES-DSG3	8.413E-07	1.765E-06	2.042E-06	2.155E-06	2.235E-06	2.280E-06
NS-DSG3	3.293E-06	2.705E-06	2.481E-06	2.410E-06	2.382E-06	2.365E-06
DSG3	6.385E-07	1.493E-06	1.847E-06	2.015E-06	2.107E-06	2.163E-06

and Mesh 3 is finer than Mesh 2. The nodal spacing of Mesh 1 and Mesh 2 is denoted as h_1 and the nodal spacing of Mesh 1 and Mesh 2 is denoted as h_2 .

2. Choose one array of $\alpha \in [0, 2]$, for example $\alpha = [0 \ 0.2 \ 0.4 \ 0.6 \dots \ 1.8 \ 2.0]$. Two different strain energy curves $E_1(\alpha) \sim \alpha$ and $E_2(\alpha) \sim \alpha$ are obtained using Mesh 1 and Mesh 2 based on Eq. (78).
3. Find the intersection point of the two strain energy curves and named this intersection point as $\alpha_1(h_1)$.
4. Obtain another intersection point $\alpha_2(h_2)$ using Mesh 2 and Mesh 3 through steps 2–3.
5. Then the unknown constants β and γ can be determined by the following equation

$$\begin{aligned} \beta &= \frac{\alpha_1(h_1) - \alpha_2(h_2)}{h_1 - h_2} \\ \gamma &= \alpha_1(h_1) - \beta h_1 \end{aligned} \quad (87)$$

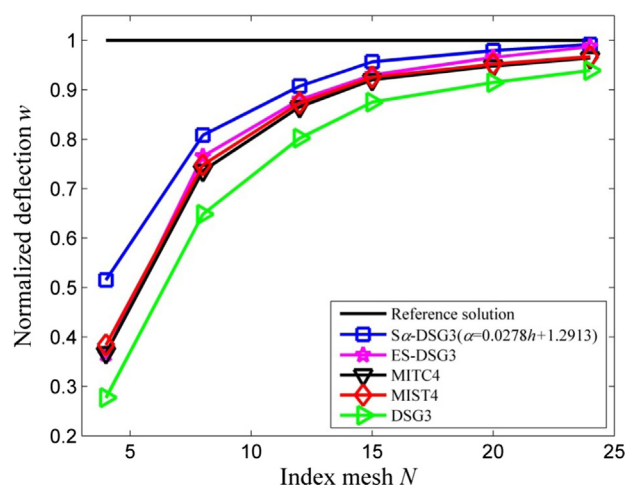


Fig. 8. The normalized displacement results obtained from different elements.

From a number of numerical examples, it is verified that the preferable $\alpha_{\text{pre}}(h)$, which is obtained through the above steps, can always work well for different sets of mesh of the same aspect ratio and results in the superconvergent solutions in both strain energy and displacement for a given problem.

4. Numerical examples

In this section, a number of typical numerical examples for the linear analysis, nonlinear analysis and free vibration analysis are performed to test the efficiency and accuracy of the present method. To make a comparison, the numerical results obtained

from several other existing shell elements such as DSG3, ESDSG3, NS-DSG3, MITC and MISTk (mixed interpolation with smoothing technique with $k = 1, 2, 4$) [29] are also presented in this paper.

4.1. Static analysis

4.1.1. Pinched cylinder with diaphragm under point load

A cylindrical shell (Young's modulus $E = 3 \times 10^7$ and Poisson's ratio $\nu = 0.3$) with rigid end diaphragm is considered as a benchmark problem. As shown in Fig. 7, the length of the cylindrical shell is $L = 600$ and the thickness is $t = 3$. The cylindrical shell is subjected to a point load $P = 1$ at the center of the cylinder and it is discretized into uniform mesh of $2 \times N \times N$ triangular elements. Only one eighth of the model is used owing to its symmetry. For the purpose of testing the exact solution property and bound property of the present model, $N = 4, 8, 12, 16, 20, 24$ are used in the computation. The reference of this problem is 1.8425×10^{-5} [56] and the following numerical results are normalized with this value. All the numerical results of the normalized displacements and strain energy for the cylindrical shell are listed in Tables 1 and 2.

In order to test the performance of the present $S\alpha$ -DSG3 model, the accuracy of solutions from different models is compared and discussed here. Following the steps given in Section 3.4, the preferable α is found to be $\alpha_{\text{pre}} = 0.0278h + 1.2913$. The normalized displacement results of $S\alpha$ -DSG3 at the center of the cylinder are shown in Fig. 8. With the aim of giving a comparison, the results of MITC4, MIST4, DSG3, and ES-DSG3 are also presented in the figure. From the figure, it is observed that the $S\alpha$ -DSG3 model can provide much better results than DSG3. More importantly, $S\alpha$ -DSG3 can even produce more accurate results than the MITC4 and MIST4, which have been proved to be very effective for shell analysis with quadrilateral elements. Furthermore, the results of $S\alpha$ -DSG3 are even better than the ES-DSG3, which is the “star ele-

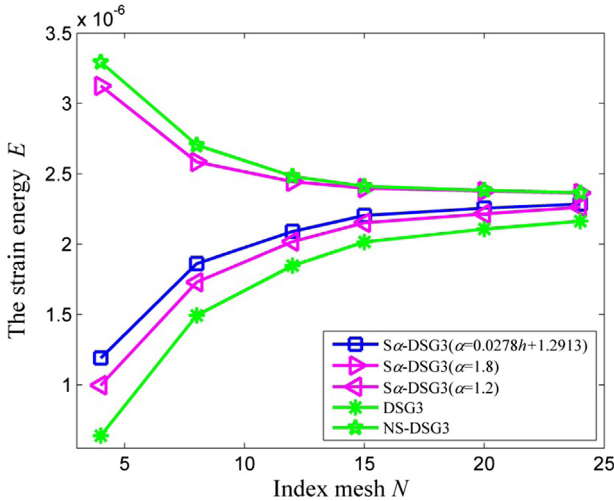


Fig. 9. The convergence of strain energy obtained from $S\alpha$ -DSG3 with different α .

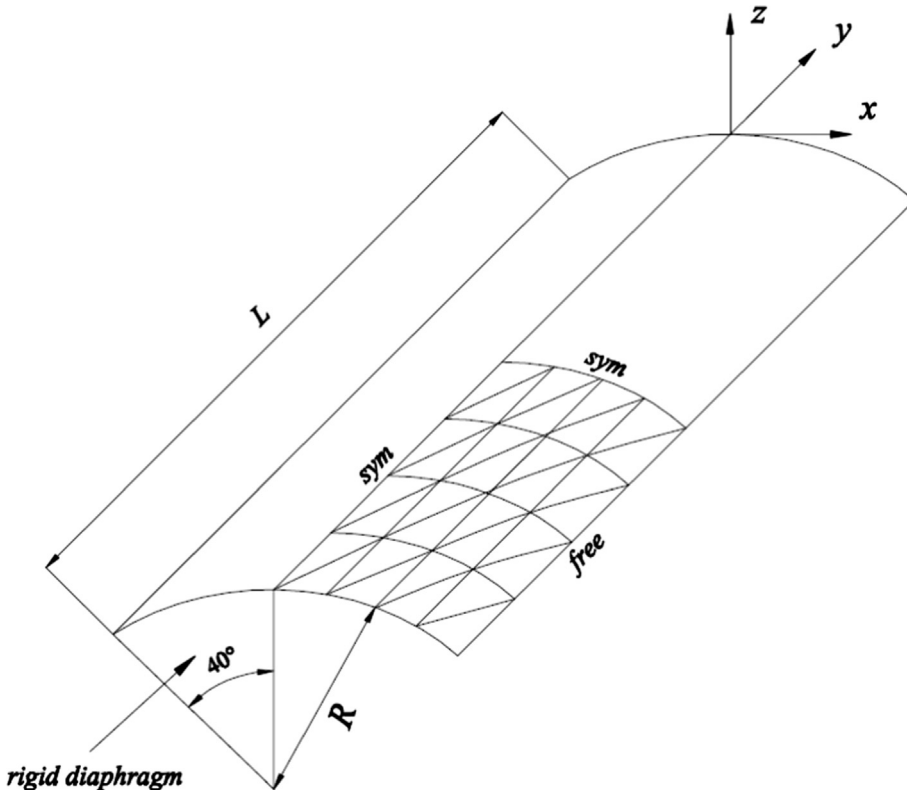


Fig. 10. The geometry of the Scordelis-Lo roof.

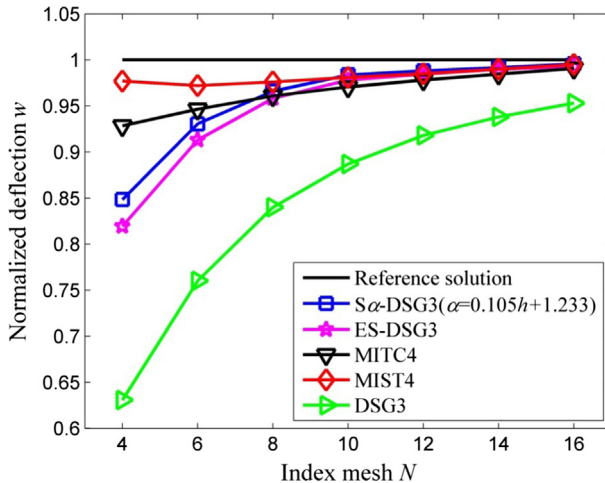


Fig. 11. The comparison of the normalized displacement results of $S\alpha$ -DSG3 with other elements.

ment" in the smoothed finite element family. The possible cause of this is that the original piecewise constant strain field of FEM is replaced by the novel linear strain field of $S\alpha$ -FEM-DSG3, which can be more effective to describe the exact strain field. This example shows that the $S\alpha$ -DSG3 can provide very accurate solution and possesses the superconvergence property.

Then the properties of $S\alpha$ -DSG3 are studied here. The strain energy obtained from $S\alpha$ -DSG3 with different α are plotted in Fig. 9. Note that the standard FEM and NS-FEM can usually provide lower and upper bounds solution for the exact one to the elasticity problems, respectively [4,57,58]. The strain energy from DSG3 and NS-DSG3 are also plotted in the figure for comparison. From the figure, it is seen that the strain energy results of $S\alpha$ -DSG3 lie exactly in between the DSG3 and NS-DSG3, and the "overly-stiff" solution and the "overly-soft" solution can be achieved when $\alpha = 1.2$ and $\alpha = 1.8$, respectively. It is not difficult to understand the above phenomenon. Actually, the stiffness of the $S\alpha$ -DSG3 model is a quadratic function of the parameter α , when α varies, a continuous solution function from "overly-stiff" solution to "overly-soft" solution can be obtained. Therefore, it can be concluded that the "close-to-exact" solution can be obtained in the

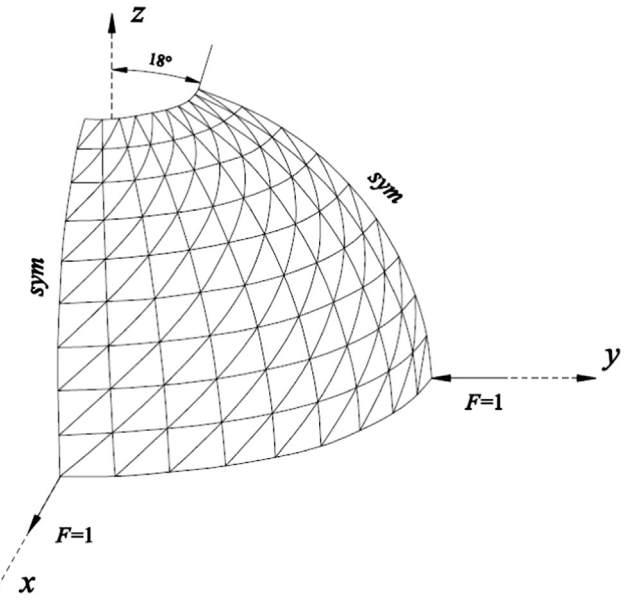


Fig. 12. The configuration of the hemispherical shell with an 18° hole under anti-symmetrical point load.

$S\alpha$ -DSG3 model by carefully choosing the value of the crucial parameter α . In addition, note that the shell considered in this example is very thin, the above results also confirm that the present $S\alpha$ -DSG3 model is free of shear locking.

4.1.2. Scordelis-Lo roof under uniform load

In this example, a benchmark problem of a cylindrical concrete shell roof known as Scordelis-Lo roof is investigated to demonstrate the excellent properties of the proposed $S\alpha$ -DSG3 model. As shown in Fig. 10, two curved edges of the roof are supported by rigid diaphragms and the other two edges are free. The material parameters of the roof are chosen as Young's modulus $E = 4.32 \times 10^8$ and Poisson's ratio $\nu = 0$. The cylindrical concrete shell roof (length $L = 50$, radius $R = 25$ and thickness $t = 0.25$) is subjected to the self-weight $q = 90$ per unit area in the z -direction. This benchmark problem is first modeled by McNeal and Harder [59] and the reference solution of the mid-side vertical

Table 3
Numerical results of the strain energy for the Scordelis-Lo roof.

Methods	Mesh						
	4×4	6×6	8×8	10×10	12×12	14×14	16×16
$S\alpha$ -DSG3 ($\alpha_{\text{pre}} = 0.105h + 1.233$)	1.028E+03	1.131E+03	1.185E+03	1.212E+03	1.217E+03	1.221E+03	1.225E+03
ES-DSG3	1.003E+03	1.110E+03	1.148E+03	1.205E+03	1.213E+03	1.218E+03	1.221E+03
MITC4	1.125E+03	1.159E+03	1.181E+03	1.194E+03	1.204E+03	1.211E+03	1.218E+03
MIST1	1.446E+03	1.313E+03	1.270E+03	1.252E+03	1.245E+03	1.242E+03	1.242E+03
MIST2	1.300E+03	1.249E+03	1.234E+03	1.229E+03	1.229E+03	1.230E+03	1.232E+03
MIST4	1.189E+03	1.193E+03	1.202E+03	1.208E+03	1.214E+03	1.219E+03	1.224E+03
DSG3	7.348E+02	9.053E+02	1.008E+03	1.069E+03	1.108E+03	1.134E+03	1.152E+03

Table 4
Numerical results of the strain energy for the hemispherical shell.

Methods	Mesh				
	4×4	6×6	8×8	12×12	16×16
$S\alpha$ -FEM-DSG3 ($\alpha_{\text{pre}} = 0.117h + 1.294$)	0.468	0.679	0.750	0.926	0.989
ES-DSG3	0.354	0.617	0.716	0.913	0.988
NS-DSG3	1.870	1.663	1.536	1.410	1.323
DSG3	0.169	0.392	0.527	0.735	0.849
ANS6S	0.949	—	0.982	0.995	1.001
S3R	0.357	—	0.913	0.968	0.981

displacement is 0.3024. Due to symmetry of this problem, only a quarter of the shell is modeled. The problem domain is divided into uniform mesh of $2 \times N \times N$ three-node triangular elements with $N = 4, 6, 8, 10, 12, 14, 16$. Following the steps given in Section 3.4, the preferable α of this problem is found to be $\alpha_{\text{pre}} = 0.105h + 1.233$. The comparison of the normalized displacement results of S α -DSG3 with other elements are shown in Fig. 11. From the figure, it is obvious that the S α -DSG3 elements are much more accurate than DSG3 and even more accurate than ES-DSG3. For very coarse mesh, the S α -DSG3 is not as effective as the MITC4 and MIST4. However, when the mesh gets finer, S α -DSG3 solutions will converge quickly and the accuracy of S α -DSG3 even surpasses

MITC4 and MIST4. This example again demonstrates that the S α -DSG3 perform better than DSG3 and can provide a superconvergent solution for shell analysis. Furthermore, the strain energy results from S α -DSG3 and other elements are listed in Table 3. From the table, similar conclusions can be obtained.

4.1.3. Hemispherical shell with an 18° hole under anti-symmetrical point load

In this section, the third benchmark problem is concerned with a hemispherical shell (radius $R = 10$ and thickness $t = 0.04$) with an 18° hole subjected to anti-symmetrical point load $F = 1$. This well-known benchmark problem is capable to test the ability of an element to handle rigid body rotations about normal to the shell surface. The configuration and mesh of the hemispherical shell is shown in Fig. 12. The material parameters are chosen as Young's modulus $E = 6.825 \times 10^7$ and Poisson's ratio $\nu = 0.3$. Symmetric boundary conditions are imposed on the right and left edges, and the other edges are free. The reference solution of the radial deflection at point load is 0.0924 [59] and the uniform mesh of $2 \times N \times N$ triangular elements with $N = 4, 6, 8, 12, 16$ are used in practical computation. For this example, the preferable α is obtained to be $\alpha_{\text{pre}} = 0.117h + 1.294$. The normalized displacements obtained from different elements are shown in Table 4. From the table, it can be found that the S α -DSG3 solutions agrees well with the reference solutions (ANS6S [60] and S3R [37]) and are more accurate than the DSG3, even a little more accurate than ES-DSG3. This example again verifies that the present S α -DSG3 is very effective and can be used to analyze the shell structures with very complicated geometries.

4.2. Convergence studies

In this section, the convergence studies will be performed to investigate the behavior of the present method. Several typical problems will be considered here. In order to measure the numerical solutions errors clearly, the following well-established s-norm proposed by Hiller and Bathe [61] will be employed here.

$$\|\mathbf{u} - \mathbf{u}_h\|_s^2 = \int_{\Omega} \Delta \boldsymbol{\varepsilon} \Delta \boldsymbol{\tau} d\Omega \quad (88)$$

where

$$\Delta \boldsymbol{\varepsilon} = \boldsymbol{\varepsilon} - \boldsymbol{\varepsilon}_h, \quad \Delta \boldsymbol{\tau} = \boldsymbol{\tau} - \boldsymbol{\tau}_h \quad (89)$$

Fig. 13. The fully clamped square plate subjected to uniform load. (a) Geometry configuration. (b) Mesh patterns.

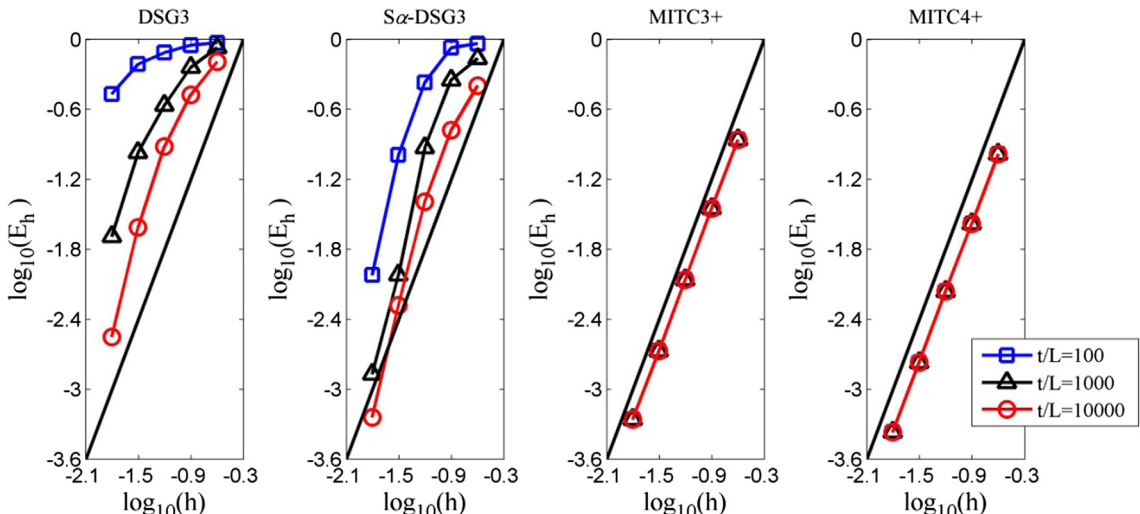


Fig. 14. The convergence rate curves for the clamped square plate using different elements.

in which \mathbf{u} is the exact solution and \mathbf{u}_h is the numerical solution, the superscript h denotes the solutions from numerical method. $\boldsymbol{\varepsilon}$ and $\boldsymbol{\tau}$ are the strain and stress vectors, respectively.

In practical computation, we usually use the reference solution \mathbf{u}_{ref} obtained from finite element solution using a very fine mesh to replace the exact solution \mathbf{u} . Then the s-norm described in Eq. (88) can be expressed as

$$\|\mathbf{u}_{ref} - \mathbf{u}_h\|_s^2 = \int_{\Omega_{ref}} \Delta \boldsymbol{\varepsilon} \Delta \boldsymbol{\tau} d\Omega_{ref} \quad (90)$$

where

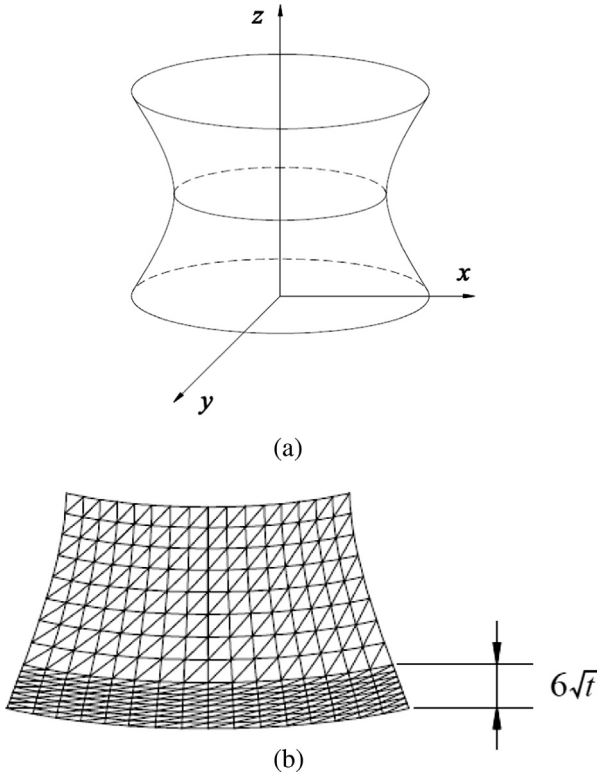


Fig. 15. The hyperboloid shell problem. (a) Geometry configuration. (b) Mesh patterns.

$$\Delta \boldsymbol{\varepsilon} = \boldsymbol{\varepsilon}_{ref} - \boldsymbol{\varepsilon}_h, \quad \Delta \boldsymbol{\tau} = \boldsymbol{\tau}_{ref} - \boldsymbol{\tau}_h \quad (91)$$

The relative error E_h is given by

$$E_h = \frac{\|\mathbf{u}_{ref} - \mathbf{u}_h\|^2}{\|\mathbf{u}_{ref}\|^2} \quad (92)$$

It is known that the optimal convergence rate for shell element is given by [9,10,61]:

$$E_h \cong Ch^k \quad (93)$$

where the constant C is independent of the shell thickness and h denotes the element size. For the three-node triangular shell element considered here, $k = 2$.

4.2.1. Fully clamped square plate

As shown in Fig. 13, the length of the square plate is $2L$ ($L = 1$) and the thickness is t . The material parameters of the plate are given by Young's modulus $E = 1.7472 \times 10^7$ and Poisson's ratio $\nu = 0.3$. Due to the symmetry, only one-quarter of the plate is modeled. The $2 \times N \times N$ uniform meshes with $N = 4, 8, 16, 32, 64$ are employed here. Fig. 14 shows the convergence rate curves of DSG3 and S α -DSG3 elements. In order to give a comparison, the results from MITC3+ element [10] and MITC4+ element [13] are also plotted in the figure. From the results, it is seen that the S α -DSG3 is not as good as MITC3+ and MITC4+. However, S α -DSG3 performs much better than DSG3. It is verified that the performance of the DSG3 element has been improved significantly by the method proposed in this paper.

4.2.2. Hyperboloid shell problem

Another numerical example is a hyperboloid shell problem shown in Fig. 15. The mid-surface of this shell structure is described by

$$x^2 + z^2 = 1 + y^2, \quad y \in [-1, 1] \quad (94)$$

The following smoothly varying load is imposed on the structure

$$p(\theta) = p_0 \cos(2\theta) \quad (95)$$

where θ is the polar angle and $p_0 = 1$.

The material parameters of this structure are Young's modulus $E = 2 \times 10^{11}$ and Poisson's ratio $\nu = 1/3$. Using symmetries, only one eighth of the structure is modeled. In order to study the different

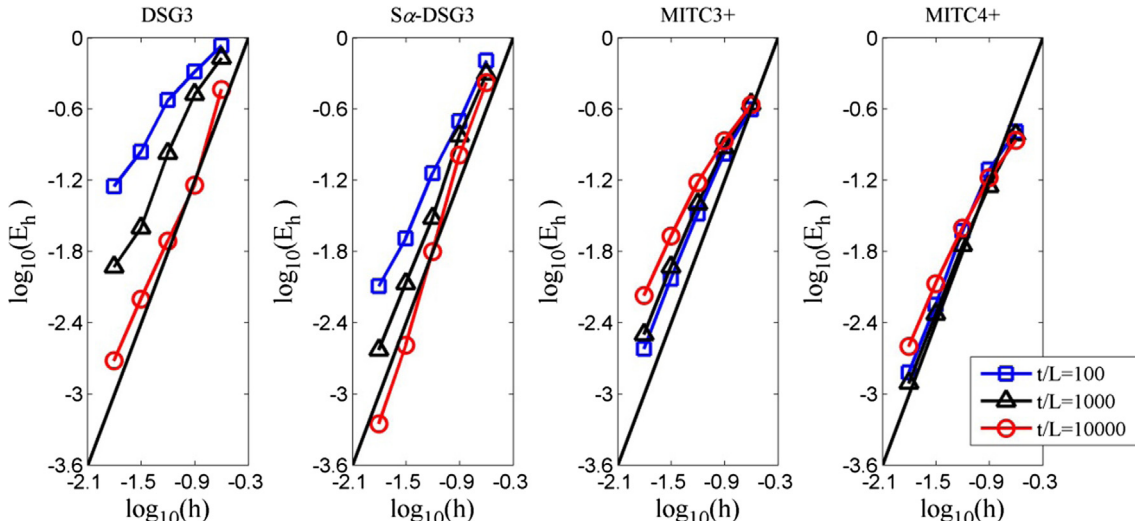


Fig. 16. The convergence rate curves for the clamped hyperboloid shell using different elements.

asymptotic behaviors of this structure. Both free boundary condition and clamped boundary condition are considered here. As shown in Fig. 15, the $2 \times N \times N$ uniform triangular meshes with $N = 4, 8, 16, 32, 64$ are used. For the clamped case, half of the mesh is used in the boundary layer of width $6\sqrt{t}$. For the free case, the boundary layer is not specially meshed.

The convergence rate curves for the clamped hyperboloid shell are plotted in Fig. 16. It is found that both DSG3 and S α -DSG3 can provide good convergence behavior which is similar to MITC3+ and MITC4+. Though S α -DSG3 is not as good as MITC3+ and MITC4+, however, the S α -DSG3 behaves much better than DSG3. The convergence rate curves for the free hyperboloid shell are shown in Fig. 17. It can be seen from the figure that the performance of the S α -DSG3 is worse than the MITC3+ and MITC4+. However, the behaviors of S α -DSG3 are much better than DSG3.

4.3. Computational efficiency study

From the numerical examples discussed in previous sections, we have known that the present S α -DSG3 can provide more accurate results than DSG3. However, it does not mean that the S α -DSG3 is more efficient than DSG3 since the formulation of S α -DSG3 is significantly more complicate. Now we will consider the computational efficiency of the present S α -DSG3 compared with DSG3. The clamped square plate discussed in Section 4.2.1 will be considered here. All the geometry configuration, material properties and mesh patterns are unchanged. All the program used in this work are compiled by a personal computer with Intel (R) Core (TM) 2 Duo CPU 2.2 GHz and RAM 4 GB. Fig. 18 illustrates the CPU time against the average mesh size for the clamped square plate. It is seen that the computational cost of S α -DSG3 is a little larger than ES-DSG3 and DSG3. This is not difficult to understand because the complicate formulation of S α -DSG3 requires more node information to assemble the element stiffness matrix. Then the bandwidth of the S α -DSG3 stiffness matrix is always larger than ES-DSG3 and DSG3. Therefore, S α -DSG3 always needs more time than ES-DSG3 and DSG3 with the same mesh. However, when the relative error is taken into consideration, it is shown that the present S α -DSG3 will exhibit higher computational efficiency than ES-DSG3 and DSG3. These useful findings can be seen in Fig. 19.

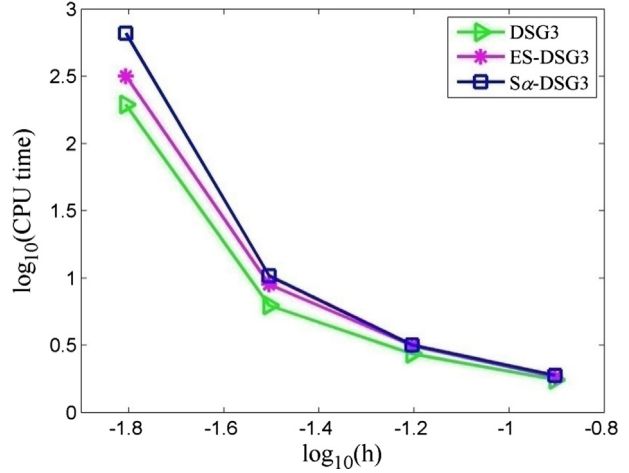


Fig. 18. The CPU time against the average mesh size for the clamped square plate.

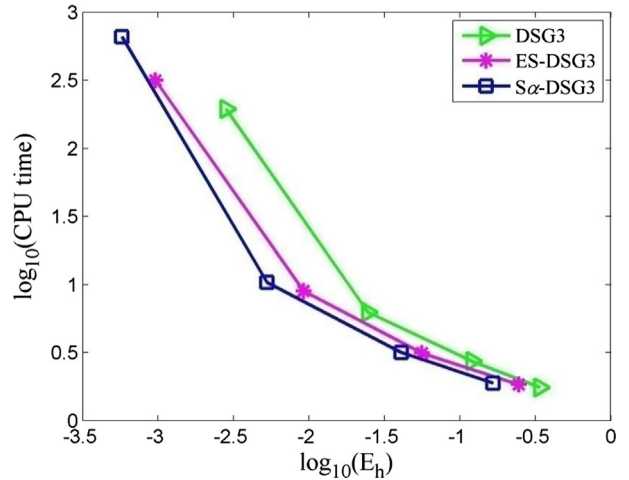


Fig. 19. The CPU time against the relative errors for the clamped square plate.

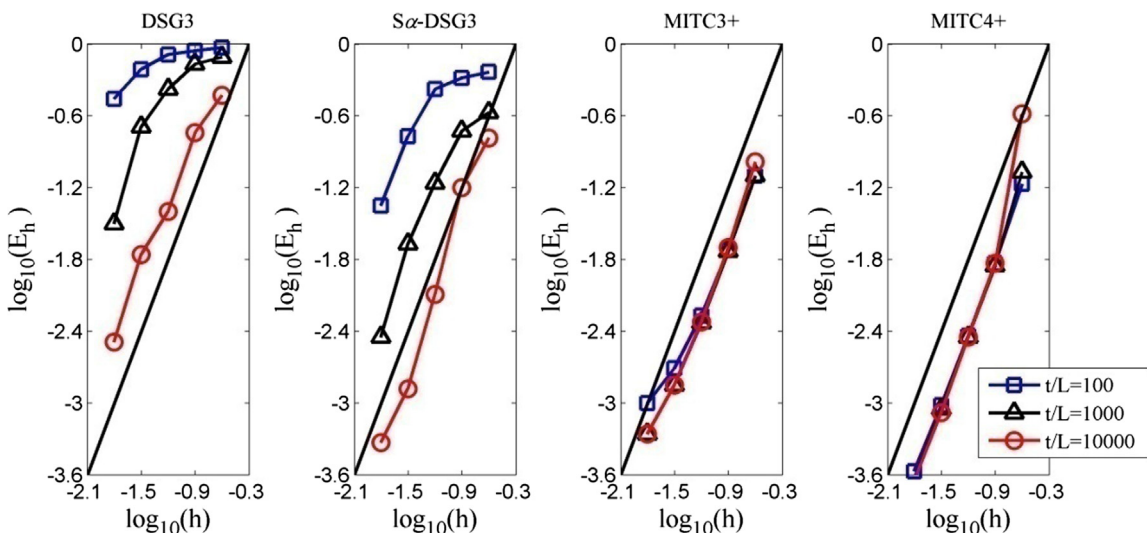


Fig. 17. The convergence rate curves for the free hyperboloid shell using different elements.

4.4. Free vibration analysis

In this section, free vibration analysis of shell structures is performed using the proposed $S\alpha$ -DSG3 model. From the numerical experiments discussed in the previous sections, it is observed that the value of preferable α (α_{pre}) varies in the interval of [1.5–1.7]. Here we directly choose $\alpha_{\text{pre}} = 1.6$ for all the numerical examples.

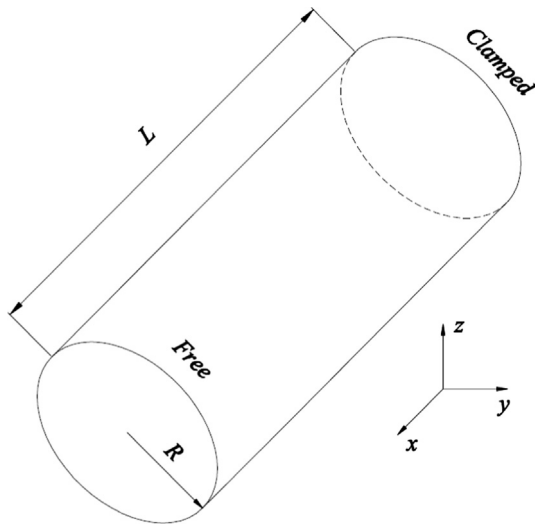


Fig. 20. The cylindrical shell with clamped-free ends.

Although this value of α may not be optimal and the solution may not be very close to the exact one, the obtained results are still very accurate. In order to give a comparison, the results from other existing elements such as DKT [62], MITC4 [63], CS-DSG3 [64], and ES-DSG3 are also available in this paper.

4.4.1. A cylindrical shell with clamped-free ends

As shown in Fig. 20, the first example is a cylindrical shell (length to radius ratios $L/R = 10$ and radius to thickness ratios $R/t = 100$) with clamped boundary condition at one edge and free at the other edge. The material parameters of the cylindrical shell are given by Young's modulus $E = 2.1 \times 10^{11}$, Poisson's ratio $\nu = 0.3$ and the mass density $\rho = 7800$. The non-dimensional frequency parameter $\bar{\omega} = 100\omega R\sqrt{\rho(1-\nu^2)/E}$ is defined to illustrate the numerical results from different elements. The $2 \times N \times N$ uniform meshes with $N = 8, 12, 16, 20$ are employed to study the natural frequencies of the cylindrical shell. The results of the eight lowest non-dimensional frequency of the shell are listed in Table 5. From the table, it is obvious that all the results obtained using the different elements are in good consistent with the analytical solution by Leissa [65] and the numerical results of RSQ20 and RSQ24 quadrilateral elements [66]. While compared to the DSG3, MIN3 and DKT, the present $S\alpha$ -DSG3 can provide much more accurate results. More importantly, $S\alpha$ -DSG3 can even produce better results than CS-DSG3 and ES-DSG3, and can be competitive with the well-known MITC4 element. Additionally, it is found that all the results from the numerical methods are larger than the analytical solutions. This may result from the “overly-stiff” features of FEM. However, the results from the proposed $S\alpha$ -DSG3 are always smaller than other elements and closer to the exact solutions. This indi-

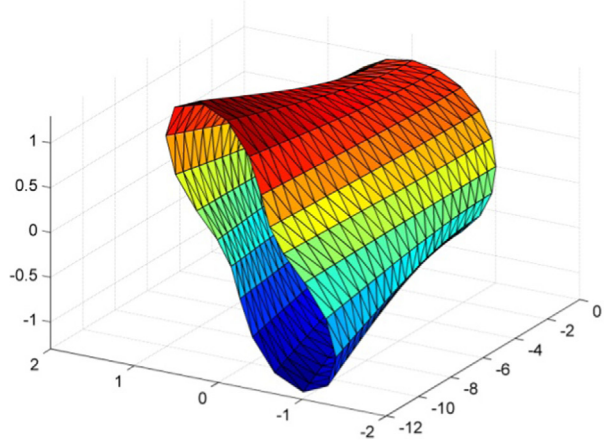
Table 5
Numerical results of non-dimensional frequency parameter $\bar{\omega}$ for the cylindrical shell.

Mesh	Methods	Mode							
		1	2	3	4	5	6	7	8
8 × 8	DKT	1.472	1.489	2.390	2.402	3.096	3.174	6.194	6.524
	MITC4	1.339	1.344	2.206	2.214	4.168	4.250	5.305	5.375
	MIN3	1.805	1.811	2.393	2.406	3.694	3.819	6.784	6.858
	DSG3	1.543	1.560	2.390	2.403	4.235	4.322	6.709	6.825
	CS-DSG3	1.456	1.475	2.390	2.402	2.962	3.006	5.748	5.971
	ES-DSG3	1.367	1.375	2.262	2.268	4.565	4.633	5.580	5.643
	$S\alpha$ -FEM-DSG3	1.316	1.328	2.121	2.134	4.118	4.286	5.302	5.504
12 × 12	DKT	1.253	1.256	2.303	2.306	2.649	2.662	4.549	4.578
	MITC4	1.188	1.189	2.213	2.214	2.926	2.936	4.013	4.025
	MIN3	2.007	2.014	2.312	2.315	4.005	4.044	5.556	5.556
	DSG3	1.281	1.285	2.303	2.306	2.989	2.998	4.786	4.814
	CS-DSG3	1.249	1.253	2.303	2.306	2.621	2.628	4.539	4.571
	ES-DSG3	1.181	1.184	2.262	2.263	2.826	2.846	4.050	4.058
	$S\alpha$ -FEM-DSG3	1.154	1.160	2.186	2.187	2.630	2.674	3.925	3.938
16 × 16	DKT	1.176	1.177	2.269	2.270	2.469	2.473	3.884	3.893
	MITC4	1.138	1.138	2.216	2.216	2.598	2.601	3.586	3.590
	MIN3	2.286	2.287	2.399	2.403	4.666	4.684	5.464	5.471
	DSG3	1.191	1.192	2.269	2.270	2.632	2.634	4.003	4.012
	CS-DSG3	1.175	1.176	2.269	2.270	2.463	2.465	3.883	3.893
	ES-DSG3	1.126	1.127	2.243	2.243	2.503	2.510	3.540	3.543
	$S\alpha$ -FEM-DSG3	1.109	1.111	2.199	2.200	2.389	2.404	3.447	3.454
20 × 20	DKT	1.140	1.140	2.252	2.253	2.383	2.384	3.593	3.596
	MITC4	1.115	1.115	2.217	2.217	2.459	2.460	3.403	3.405
	MIN3	2.279	2.279	2.845	2.848	5.443	5.452	5.534	5.535
	DSG3	1.149	1.150	2.253	2.253	2.479	2.480	3.665	3.669
	CS-DSG3	1.139	1.140	2.252	2.253	2.383	2.384	3.593	3.597
	ES-DSG3	1.101	1.102	2.228	2.228	2.378	2.381	3.340	3.342
	$S\alpha$ -FEM-DSG3	1.093	1.094	2.206	2.206	2.312	2.319	3.286	3.289
Leissa		1.109		2.458					
RSQ20		1.092		2.237		2.237			
RSQ24		1.101		2.237		2.277			

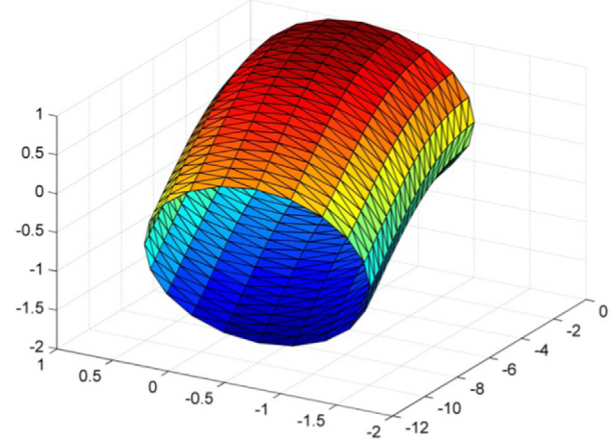
cates that the reconstructed novel linear strain field used in the S α -DSG3 model possesses proper stiffness and can achieve better solutions. Furthermore, the first six shape modes of the cylindrical shell using S α -DSG3 are plotted in Fig. 21. It is clear that S α -DSG3 is very stable and has no spurious non-zero-energy modes.

4.4.2. A hemispherical panel

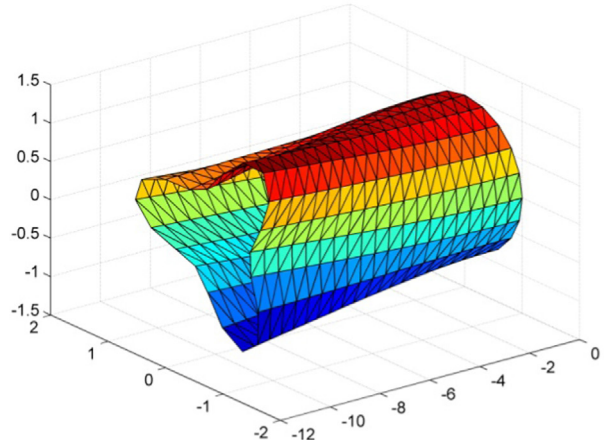
The second benchmark problem is a hemispherical panel ($E = 2.1 \times 10^{11}$, Poisson's ratio $\nu = 0.3$ and the mass density $\rho = 7800$) with two clamped edges and two free edges. As shown in Fig. 22, the geometric parameters of the hemispherical panel



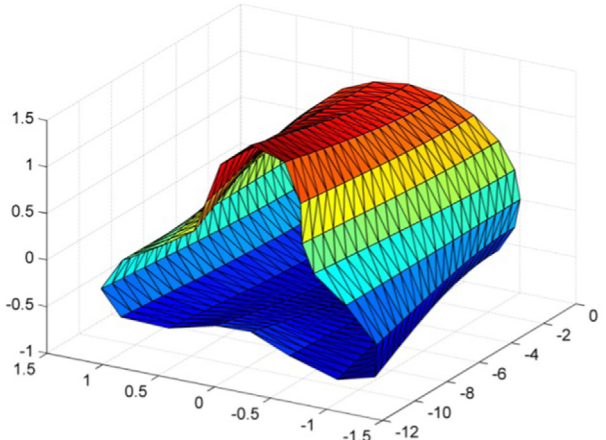
(a) Mode 1



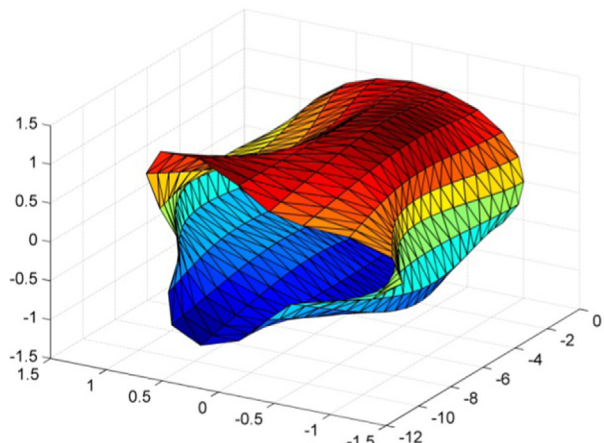
(b) Mode 2



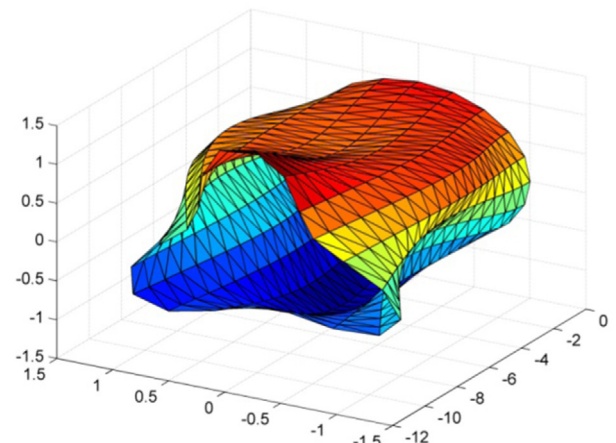
(c) Mode 3



(d) Mode 4



(e) Mode 5



(f) Mode 6

Fig. 21. The first six shapes modes of the cylindrical shell by the S α -DSG3 with the $2 \times 20 \times 20$ mesh.

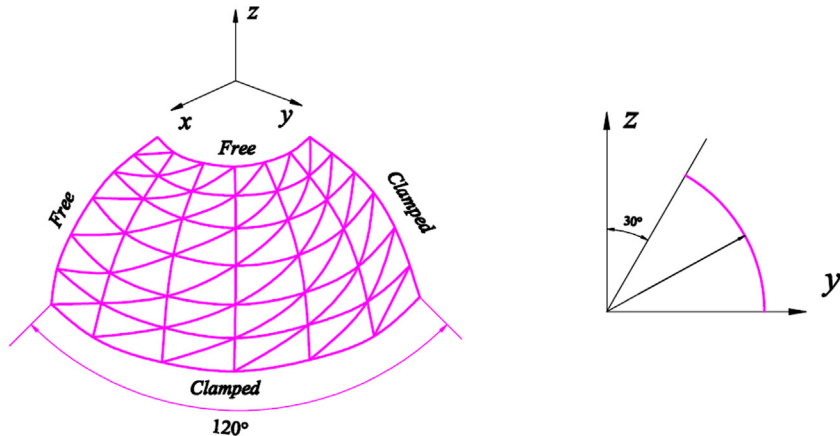


Fig. 22. The geometry of a hemispherical panel with two clamped edges and two free edges.

are $R = 1$, thickness $t = 0.1$. Uniform meshes of $2 \times N \times N$ elements with $N = 8, 12, 16, 20$ are used in this example. The lowest eight natural frequencies (Hz) of the hemispherical panel with different elements are listed in Table 6. In order to give a comparison, the reference solution from GDQ [67] and commercial software packages such as Ansys, Abaqus, Nastran and Straus are also presented in the table. It is seen from the table that the present S α -DSG3 shows excellent performance and can provide high accuracy solutions compared to other elements. The first six shape modes of the panel by S α -DSG3 are shown in Fig. 23 and it is found that all the shapes express exactly the real physical model of the panel.

4.5. Geometric nonlinear analysis

In this section, two typical benchmark problems are investigated to assess the performance of the present method in geometric nonlinear analysis. For nonlinear analysis, it is generally difficult to obtain the “exact” α for all loading stages. Similarly to

the free vibration problems, an $\alpha \in [1.5–1.7]$ is recommended and $\alpha = 1.6$ is used here. The numerical tests so far shown that the using of such an α can usually provide more accurate results than the DSG3. Of course, the α chosen here is not optimal for the nonlinear problem and we will not obtain a nearly exact solution, but the accuracy of the DSG3 solution is still significantly improved.

4.5.1. Cantilever plate subjected to shear force

The first numerical example is a cantilever plate subjected to shear force shown in Fig. 24. This problem has been considered many times [12,68,69]. The material properties of this plate are Young's modulus $E = 2 \times 10^{11}$ and Poisson's ratio $\nu = 0$. The geometry configurations are length $L = 10$, width $B = 1$ and thickness $t = 0.1$. The end shear force we used is $P_{\max} = 4$. The vertical and horizontal displacements at the end against the end shear force are shown in Fig. 25. In order to give a comparison, the numerical results from different elements are plotted in the figure. Among

Table 6
Numerical results of natural frequencies for the hemispherical panel.

Mesh	Methods	Mode							
		1	2	3	4	5	6	7	8
8 × 8	DKT	359.3	496.4	777.5	1009	1178	1465.2	1506.5	1671.3
	MITC4	332.5	471.3	729	950.7	1102.9	1392.7	1420.6	1520.9
	CS-DSG3	346.3	472.4	750.6	983.4	1136.4	1378.1	1450.1	1585.1
	ES-DSG3	341.13	471.05	741.86	969.19	1120.4	1369.8	1433.6	1566.1
	S α -FEM-DSG3	335.74	470.13	735.14	957.99	1110	1363.8	1424.5	1551.9
12 × 12	DKT	350.6	487.1	755.1	960.8	1130.8	1398.7	1451.3	1566.9
	MITC4	328.9	464.5	715.7	917.3	1073.4	1334.5	1367	1447.4
	CS-DSG3	338.3	467	731.6	933.03	1089.6	1346.1	1368.2	1475.6
	ES-DSG3	333.57	465.92	720.71	927.21	1084.7	1342.3	1358.8	1458.6
	S α -FEM-DSG3	331.01	464.29	714.78	923.16	1081.9	1340.1	1349.3	1448.2
16 × 16	DKT	346.4	483.2	745	942	1113.3	1368.4	1429.8	1529.5
	MITC4	328	462.6	711.5	906.1	1064.4	1311.5	1349.5	1424.1
	CS-DSG3	334.4	464.1	722.4	913.7	1071.8	1329.1	1331.4	1436.2
	ES-DSG3	331.4	464.05	717.67	907.34	1069.5	1322.5	1329.2	1430.2
	S α -FEM-DSG3	329.83	463.15	712.88	903.88	1066.9	1317.3	1326.3	1426.5
20 × 20	DKT	344.2	481.2	739.7	932.8	1105	1352.6	1419.3	1512.8
	MITC4	327.7	461.8	709.7	901.1	1060.7	1300.7	1342	1414.2
	CS-DSG3	332.2	462.4	717.3	904.1	1063.2	1309.2	1323.1	1417.6
	ES-DSG3	328.99	462.29	712.16	903.63	1062.9	1306	1322.9	1414.7
	S α -FEM-DSG3	328.25	462.19	711.13	901.8	1061.8	1302.9	1322.7	1406.1
	Abaqus	326.94	459.01	706.98	884.09	1047.6	1270.8	1309.2	1383.7
	Ansys	328.48	460.89	710.52	893.51	1056.1	1285.2	1328	1404
	Nastran	328.69	460.93	711.09	892.71	1055.8	1282.4	1325.9	1401.9
	Straus	327.28	458.54	706.64	888.86	1049.5	1278.9	1313.9	1395.5
	GDQ	327.39	458.58	705.71	885.18	1046.6	1270.7	1305.1	1382.8

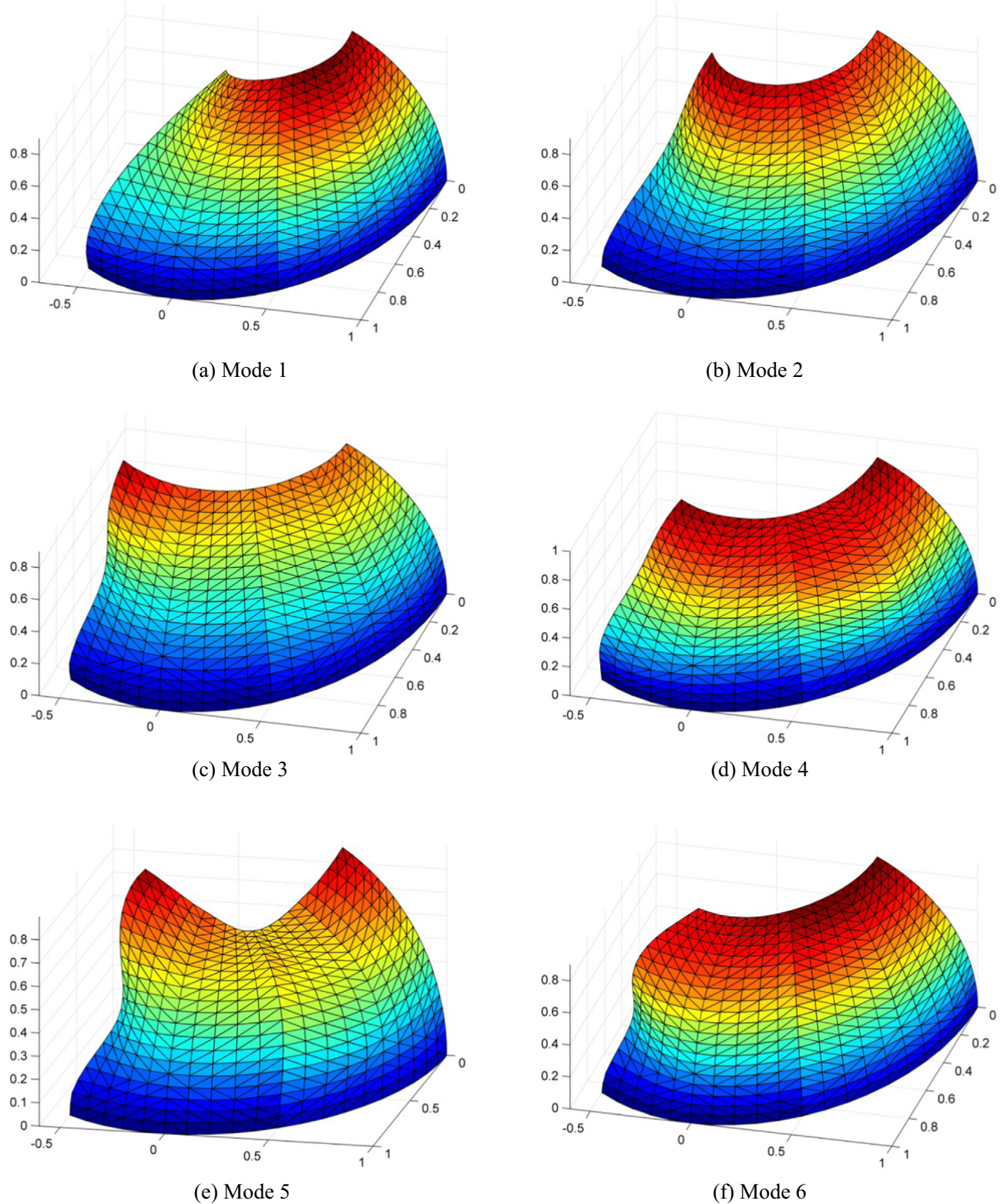


Fig. 23. The first six shapes modes of the hemispherical panel by the S α -DSG3 with the $2 \times 20 \times 20$ mesh.

them, the results from MITC shell elements (including MITC4, MITC3 and MITC3+) are from Ref. [12]. The reference solutions are numerical results using a very fine mesh. From the figure, it is seen that the S α -DSG3 results are a little worse than the MITC results. However, the S α -DSG3 behaves much better than the original DSG3.

4.5.2. Clamped circular plate subjected to uniform load

The second numerical example is a clamped circular plate. The geometry configuration and mesh of this plate are shown in Fig. 26. The radius of the plate is $R = 1$ and thickness $t = 0.1$. The material properties are chosen as Young's modulus $E = 3 \times 10^7$ and Poisson's ratio $\nu = 0.3$. The uniform load applied to the plate is $q_{\max} = 220$.

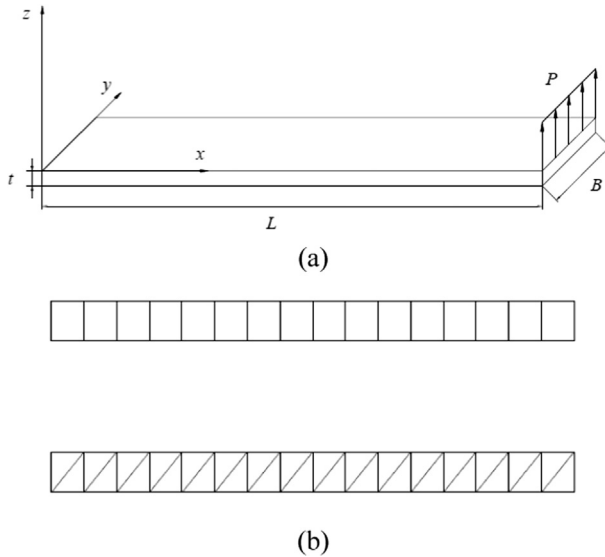


Fig. 24. The cantilever plate subjected to end shear force. (a) Geometry configuration. (b) Mesh patterns.

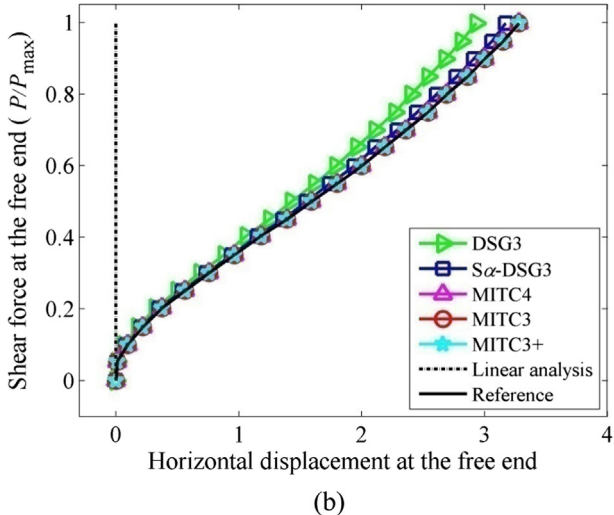
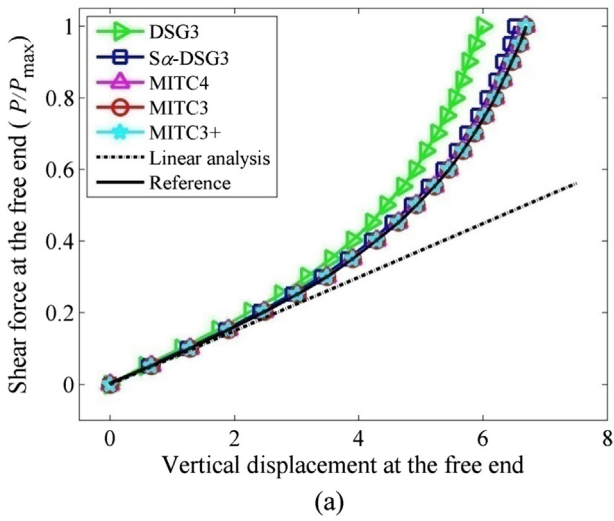


Fig. 25. The displacement results at the end against the end shear force for the cantilever plate. (a) The vertical displacement results. (b) The horizontal displacement results.

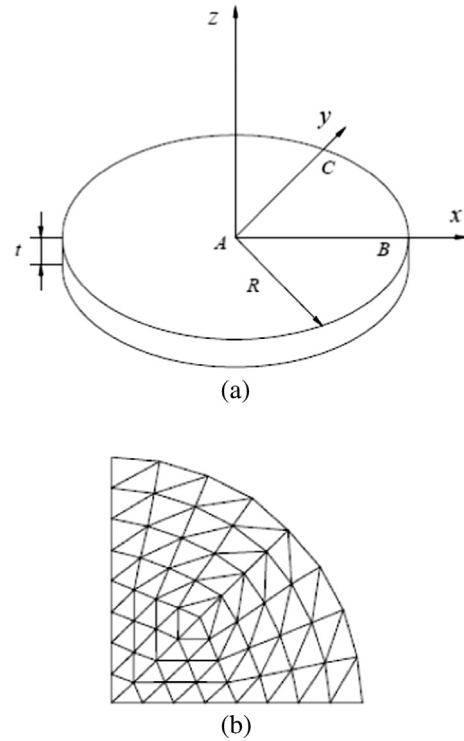


Fig. 26. The clamped circular plate. (a) The geometry configuration. (b) The mesh pattern.

Owing to the symmetry, only one quarter of the plate is modeled in practical computation. The analytical solution to this problem is available and the central deflection can be expressed as [70]:

$$\frac{qR^4}{Et^4} = \frac{16}{3(1-\nu^2)} \left[\frac{w}{t} + \frac{1}{360} (1+\nu)(173 - 73\nu) \left(\frac{w}{t} \right)^3 \right] \quad (96)$$

where w is the central deflection.

Fig. 27 shows the central deflection results versus the uniform load. The numerical results from different methods are plotted in the figure. It is observed that the present $S\alpha$ -DSG3 results are very close to the analytical solution and even a little better than ES-DSG3. More importantly, the $S\alpha$ -DSG3 is clear much better than the original DSG3.

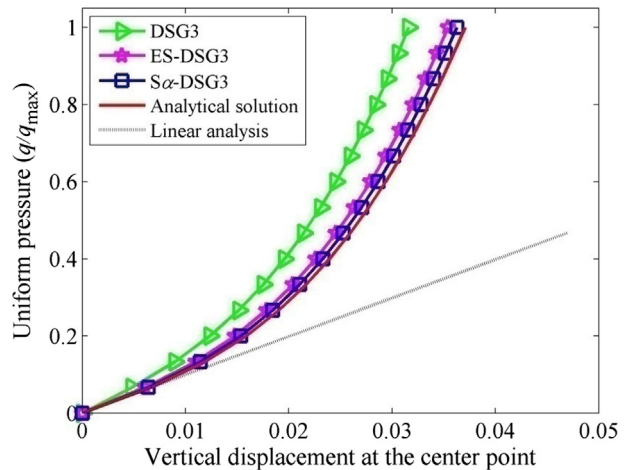


Fig. 27. The central deflection results versus the uniform load for the clamped circular plate.

5. Conclusions

In this paper, a super convergent alpha element method ($S\alpha$ FEM) based on triangular mesh is proposed for static and free vibration analysis of shell structures. The linear strain field used in the $S\alpha$ FEM model is obtained from the original piecewise constant strain field with a particular elegant procedure. In order to get rid of shear locking, the discrete shear gap technique is employed to give a superconvergent alpha discrete shear gap ($S\alpha$ -DSG3) method for shell problems. The following conclusions can be drawn from the numerical examples.

- (a) The present $S\alpha$ -DSG3 model possesses variational consistency property since it is derived from the modified Hellinger-Reissner principle which is rooted from Hu-Washizu principle.
- (b) The stiffness of the $S\alpha$ -DSG3 model is a quadratic function of the parameter α , when α varies, a continuous solution function from “overly-stiff” solution to “overly-soft” solution can be obtained. By carefully choosing the value of the crucial parameter α , the “close-to-exact” solution can be obtained from the $S\alpha$ -DSG3 model.
- (c) For linear and nonlinear analysis, the solution accuracy of the present $S\alpha$ -DSG3 is often much better than DSG3 with the same mesh and even a little better than ES-DSG3.
- (d) Although the convergence behavior of the present $S\alpha$ -DSG3 is not as good as some new MITC elements. However, the performance of original DSG3 has been improved by the present method.
- (e) For free vibration analysis, the $S\alpha$ -DSG3 is more effective than DSG3 and ES-DSG3 to predict the natural frequencies of shells with different geometries.
- (f) Since only triangular meshes, which can be automatically generated for complicated domains, are involved in the $S\alpha$ -DSG3 model, hence it has great potential in practical application.

Acknowledgements

The authors wish to express their gratitude to the National Natural Science Foundation of China (Contract No. 51379083, 51579109 and 51579112).

References

- [1] Timoshenko SP, Woinowsky-Krieger S. Theory of plates and shells. McGraw-hill; 1959.
- [2] Bathe KJ. Finite element procedures. New Jersey: Prentice-Hall; 1996.
- [3] Reddy JN. Theory and analysis of elastic plates and shells. New York: CRC Press, Taylor and Francis Group; 2006.
- [4] Liu GR, Quek SS. The finite element method, a practical course. Oxford: Butterworth Heinemann; 2003.
- [5] Liu GR. Meshfree methods: moving beyond the finite element method. Taylor & Francis; 2009.
- [6] Dvorkin EN, Bathe KJ. A continuum mechanics based four-node shell element for general non-linear analysis. Eng Comput 1984;1:77–88.
- [7] Bathe KJ, Dvorkin EN. A formulation of general shell elements-the use of mixed interpolation of tensorial components. Int J Numer Methods Eng 1986;22:697–722.
- [8] Lee Y, Yoon K, Lee PS. Improving the MITC3 shell finite element by using the Hellinger-Reissner principle. Comput Struct 2012;110–111:93–106.
- [9] Jeon HM, Lee PS, Bathe KJ. The MITC3 shell finite element enriched by interpolation covers. Comput Struct 2014;134:128–42.
- [10] Lee Y, Lee PS, Bathe KJ. The MITC3+ shell element and its performance. Comput Struct 2014;138:12–23.
- [11] Lee Y, Jeon HM, Lee PS, Bathe KJ. The modal behavior of the MITC3+ triangular shell element. Comput Struct 2015;153:148–64.
- [12] Jeon HM, Lee Y, Lee PS, Bathe KJ. The MITC3+ shell element in geometric nonlinear analysis. Comput Struct 2015;146:91–104.
- [13] Ko Y, Lee PS, Bathe KJ. The MITC4+ shell element and its performance. Comput Struct 2016;169:57–68.
- [14] Hughes TJR, Taylor RL, Kanoknukulchai W. Simple and efficient element for plate bending. Int J Numer Methods Eng 1977;11:1529–43.
- [15] Hughes TJR, Cohen M, Haroun M. Reduced and selective integration techniques in the finite element analysis of plates. Nucl Eng Des 1978;46:203–22.
- [16] Malkus DS, Hughes TJR. Mixed finite element methods-reduced and selective integration techniques: a unification of concepts. Comput Methods Appl Mech Eng 1978;15:63–81.
- [17] MacNeal RH. Derivation of element stiffness matrices by assumed strain distributions. Nucl Eng Des 1982;70:3–12.
- [18] Tessler A, Hughes TJR. A three-node Mindlin plate element with improved transverse shear. Comput Methods Appl Mech Eng 1985;50:71–101.
- [19] Kim JH, Kim YH. Three-node macro triangular shell element based on the assumed natural strains. Comput Mech 2002;29:441–58.
- [20] Bletzinger KU, Bischoff M, Ramm E. A unified approach for shear-locking-free triangular and rectangular shell finite elements. Comput Struct 2000;75:321–34.
- [21] Liu GR, Nguyen-Thoi T. Smoothed finite element methods. New York: CRC Press, Taylor and Francis, Group; 2010.
- [22] Liu GR, Nguyen-Thoi T, Dai KY, Lam KY. Theoretical aspects of the smoothed finite element method (SFEM). Int J Numer Methods Eng 2007;71:902–30.
- [23] Nguyen-Xuan H, Bordas S, Nguyen-Dang H. Smooth finite element methods: convergence, accuracy and properties. Int J Numer Methods Eng 2008;74:175–208.
- [24] Chai YB, Li W, Gong ZX, Li TY. Hybrid smoothed finite element method for two-dimensional underwater acoustic scattering problems. Ocean Eng 2016;116:129–41.
- [25] Chai YB, Li W, Gong ZX, Li TY, You XY. Analysis of underwater acoustic scattering problems using stable node-based smoothed finite element method. Eng Anal Bound Elem 2016;72:27–41.
- [26] Chen JS, Wu CT, Yoon S, You Y. A stabilized conforming nodal integration for Galerkin mesh-free methods. Int J Numer Methods Eng 2001;50:435–66.
- [27] Liu GR, Dai KY, Nguyen-Thoi T. A smoothed finite element method for mechanics problems. Comput Mech 2007;39:859–77.
- [28] Nguyen-Thanh N, Rabczuk T, Bordas S, Debongnie JF. A smoothed finite element method for plate analysis. Comput Methods Appl Mech Eng 2008;197:1184–203.
- [29] Nguyen-Thanh N, Rabczuk T, Nguyen-Xuan H, Bordas S. A smoothed finite element method for shell analysis. Comput Methods Appl Mech Eng 2008;198:165–77.
- [30] Liu GR, Zeng W, Nguyen-Xuan H. Generalized stochastic cell-based smoothed finite element method (GS-CS-FEM) for solid mechanics. Finite Elem Anal Des 2013;63:51–61.
- [31] Cui XY, Liu GR, Li GY, Zhao X, Nguyen-Thoi T, Sun GY. A smoothed finite element method (SFEM) for linear and geometrically nonlinear analysis of plates and shells. CMES-Comput Model Eng Sci 2008;28:109–25.
- [32] Nguyen-Thoi T, Vu-Do HC, Rabczuk T, Nguyen-Xuan H. A node-based smoothed finite element method (NS-FEM) for upper bound solution to visco-elastoplastic analyses of solids using triangular and tetrahedral meshes. Comput Methods Appl Mech Eng 2010;199:3005–27.
- [33] Liu GR, Nguyen-Thoi T, Nguyen-Xuan H, Lam KY. A node-based smoothed finite element method (NS-FEM) for upper bound solutions to solid mechanics problems. Comput Struct 2009;87:14–26.
- [34] Liu GR, Chen L, Nguyen-Thoi T, Zeng KY, Zhang GY. A novel singular node-based smoothed finite element method (NS-FEM) for upper bound solutions of fracture problems. Int J Numer Meth Eng 2013;83:1466–97.
- [35] Liu GR, Nguyen-Thoi T, Lam KY. An edge-based smoothed finite element method (ES-FEM) for static, free and forced vibration analyses of solids. J Sound Vib 2009;320:1100–30.
- [36] Nguyen-Xuan H, Liu GR, Thai-Hoang C, Nguyen-Thoi T. An edge-based smoothed finite element method (ES-FEM) with stabilized discrete shear gap technique for analysis of Reissner-Mindlin plates. Comput Methods Appl Mech Eng 2010;199:471–89.
- [37] Cui XY, Liu GR, Li GY, Zhang GY, Zheng G. Analysis of plates and shells using an edge-based smoothed finite element method. Comput Mech 2010;45:141–56.
- [38] Zheng G, Cui XY, Li GY, Wu SZ. An edge-based smoothed triangle element for non-linear explicit dynamic analysis of shells. Comput Mech 2011;48:65–80.
- [39] Li W, Chai YB, Lei M, Liu GR. Analysis of coupled structural-acoustic problems based on the smoothed finite element method (S-FEM). Eng Anal Bound Elem 2014;42:84–91.
- [40] Phung-Van P, Thai CH, Nguyen-Thoi T, Nguyen-Xuan H. Static and free vibration analyses of composite and sandwich plates by an edge-based smoothed discrete shear gap method (ES-DSG3) using triangular elements based on layerwise theory. Compos Pt B-Eng 2014;60:227–38.
- [41] Nguyen-Thoi T, Liu GR, Vu-Do HC, Nguyen-Xuan H. A face-based smoothed finite element method (FS-FEM) for visco-elastoplastic analyses of 3D solids using tetrahedral mesh. Comput Methods Appl Mech Eng 2009;198:3479–98.
- [42] Nguyen-Thoi T, Liu GR, Lam KY, Zhang GY. A face-based smoothed finite element method (FS-FEM) for 3D linear and geometrically non-linear solid mechanics problems using 4-node tetrahedral elements. Int J Numer Methods Eng 2009;78:324–53.
- [43] Liu GR, Nguyen-Xuan H, Nguyen-Thoi T, Xu X. A novel Galerkin-like weakform and a superconvergent alpha finite element method ($S\alpha$ FEM) for mechanics problems using triangular meshes. J Comput Phys 2009;228:4055–87.
- [44] Liu GR, Nguyen-Xuan, Nguyen-Thoi T. A variationally consistent α FEM (VC α FEM) for solution bounds and nearly exact solution to solid mechanics

- problems using quadrilateral elements. *Int J Numer Methods Eng* 2011;85:461–97.
- [45] Nguyen-Thanh N, Rabczuk T, Nguyen-Xuan H, Bordas S. An alternative alpha finite element method (A α FEM) for free and forced structural vibration using triangular meshes. *J Comput Appl Math* 2010;233:2112–35.
- [46] Nguyen-Thanh N, Rabczuk T, Nguyen-Xuan H, Bordas S. An alternative alpha finite element method with discrete shear gap technique for analysis of isotropic Mindlin-Reissner plates. *Finite Elem Anal Des* 2011;47:519–35.
- [47] Thai-Hoang C, Nguyen-Thanh N, Nguyen-Xuan H, Rabczuk T. An alternative alpha finite element method with discrete shear gap technique for analysis of laminated composite plates. *Appl Math Comput* 2011;217:7324–48.
- [48] Bonet J, Burton AJ. A simple average nodal pressure tetrahedral element for incompressible and nearly incompressible dynamic explicit applications. *Commun Numer Methods Eng* 1998;14:437–49.
- [49] Dohrmann CR, Heinstein MW, Jung J, Key SW, Witkowski WW. Node-based uniform strain elements for three-node triangular and four-node tetrahedral meshes. *Int J Numer Methods Eng* 2000;47:1549–68.
- [50] Puso MA, Solberg J. A stabilized nodally integrated tetrahedral. *Int J Numer Methods Eng* 2006;67:841–67.
- [51] Krysl P, Zhu B. Locking-free continuum displacement finite elements with nodal integration. *Int J Numer Methods Eng* 2008;76:1020–43.
- [52] Castellazzi G, Krysl P. Displacement-based finite elements with nodal integration for Reissner-Mindlin plates. *Int J Numer Methods Eng* 2009;80:135–62.
- [53] Wang D, Chen JS. Locking-free stabilized conforming nodal integration for meshfree Mindlin-Reissner plate formulation. *Comput Methods Appl Mech Eng* 2004;193:1065–83.
- [54] Wang D, Sun Y. A Galerkin meshfree formulation with stabilized conforming nodal integration for geometrically nonlinear analysis of shear deformable plates. *Int J Comput Methods* 2011;8:685–703.
- [55] Liu GR, Xu X, Zhang GY, Nguyen-Thoi T. A superconvergent point interpolation method (SC-PIM) with piecewise linear strain field using triangular mesh. *Int J Numer Methods Eng* 2009;77:1439–67.
- [56] Kasper EP, Taylor RL. A mixed-enhanced strain method: part I: geometrically linear problems. *Comput Struct* 2000;75:237–50.
- [57] Zienkiewicz OC, Taylor RL. The finite element method. Oxford, UK: Butterworth Heinemann; 2000.
- [58] Hughes TJR. The finite element method: linear static and dynamic finite element analysis. Englewood Cliffs, NJ: Prentice-Hall; 1987.
- [59] MacNeal RH, Harder RL. A proposed standard set of problems to test finite element accuracy. *Finite Elem Anal Des* 1985;1:3–20.
- [60] Sze KY, Zhu D. A quadratic assumed natural strain curved triangular shell element. *Comput Methods Appl Mech Eng* 1999;174:57–71.
- [61] Hiller JF, Bathe KJ. Measuring convergence of mixed finite element discretizations: an application to shell structures. *Comput Struct* 2003;81:639–54.
- [62] Batoz JL, Bathe KJ, Ho LW. A study of three-node triangular plate bending elements. *Int J Numer Methods Eng* 1980;15:1771–812.
- [63] Bathe KJ, Dvorkin EN. A four-node plate bending element based on Mindlin/Reissner plate theory and a mixed interpolation. *Int J Numer Methods Eng* 1985;21:367–83.
- [64] Nguyen-Thoi T, Phung-Van P, Thai-Hoang C, Nguyen-Xuan H. A cell-based smoothed discrete shear gap method (CS-DSG3) using triangular elements for static and free vibration analyses of shell structures. *Int J Mech Sci* 2013;74:32–45.
- [65] Leissa AW. Vibration of shell. Washington DC: NASA, SP-288; 1973.
- [66] Zhang YX, Cheung YK, Chen WJ. Two refined non-conforming quadrilateral flat shell elements. *Int J Numer Methods Eng* 2000;49:355–82.
- [67] Tornabene F, Viola E. Vibration analysis of spherical structural elements using the GDQ method. *Comput Math Appl* 2007;53:1538–60.
- [68] Jiang L, Chernuka MW. A simple four-noded corotational shell element for arbitrarily large rotations. *Comput Struct* 1994;53:1123–32.
- [69] To CWS, Liu ML. Hybrid strain based three node flat triangular shell elements—II. Numerical investigation of nonlinear problems. *Comput Struct* 1995;54:1057–76.
- [70] Chia CY. Nonlinear analysis of plate. New York: McGraw-Hill; 1980.